AIAA JOURNAL
Vol. 46, No. 2, February 2008

Constitutive Modeling and Simulation of Perforation of Targets by Projectiles

George Z. Voyiadjis* and Rashid K. Abu Al-Rub†
Louisiana State University, Baton Rouge, Louisiana 70803
and
Anthony N. Palazotto‡
U.S. Air Force Institute of Technology, Wright–Patterson Air Force Base, Ohio 45433-7765

DOI: 10.2514/1.26011

The effective use of existing finite element codes in the direct simulation of hypervelocity impacts by projectiles is limited by the dependence of the size of localized failure regions on the mesh size and alignment. This gives rise to a nonphysical description of the penetration and perforation processes. A micromechanical constitutive model that couples the anisotropic thermoviscodamage mechanism with the thermohypoelastoviscoplastic deformation is presented here as a remedy to this situation. Explicit and implicit microstructural length-scale measures, which preserve the well-posed nature of the differential equations, are introduced through the use of the viscosity and gradient localization limiters. Simple and robust numerical algorithms for the integration of the constitutive equations are also presented. The proposed unified integration algorithms are extensions of the classical rate-independent return-mapping algorithms to the rate-dependent problems. A simple and direct computational algorithm is also used for implementing the gradient-dependent equations. This algorithm can be implemented in the existing finite element codes without numerous modifications, compared with the current numerical approaches for integrating gradient-dependent models. Model capabilities are preliminarily illustrated for the dynamic localization of inelastic flow in adiabatic shear bands and the perforation of a 12-mm-thick Weldox 460E steel plate by a deformable blunt projectile at various impact speeds.

Introduction

THE recent advances in aerospace and war capabilities have made necessary the modification of the design of structures so that they can resist penetration and perforation by projectiles with much higher impact energies. In this respect, high-performance materials need to be developed so that they can offer significant advantages over the currently used materials. Specific mechanical properties are targeted by the aid of these new materials, such as high specific strength, high stiffness, and low coefficient of thermal expansion. Moreover, studies of hypervelocity impact phenomena are motivated by a variety of science and engineering applications [1] such as kinetic energy penetrators [2], engineering research on the design of spacecraft shielding [3], and equations of state [4]. Therefore, the high-velocity impacting mechanism needs to be understood properly to be able to design materials of high ballistic-resistant response. However, the exact mechanism by which the impacting target materials undergo fracture and ablation is a relatively complex process [5]. Generally, strong shock wave and material interactions are generated and propagated along both the projectile and the target, which can lead to fracture at low global inelastic strains. Phenomenologically, as illustrated in Fig. 1, the penetration can be viewed as a process to generate a cone-shaped macrocrack in the material, in which the kinetic energy of the penetrator is dissipated.

Presented as Paper 2089 at the 47th AIAA/ASME/ASCE/AHS/ASC Structures, Structural Dynamics, and Materials Conference, Newport, RI, 1–4 May 2006; received 19 June 2006; revision received 7 December 2006; accepted for publication 8 December 2006.

*Boyd Professor, Department of Civil and Environmental Engineering; voyiadjis@eng.lsu.edu. Associate Fellow AIAA.
†Professional-in-Residence, Department of Civil and Environmental Engineering; rabual1@lsu.edu.
‡Professor, Department of Aeronautics and Astronautics. Fellow AIAA.

Considering the relatively high cost of conducting experiments [6] that may shed some light on the design of high-performance materials under hypervelocity impacts and the wide range of design parameters requiring investigation [7], the development of improved computer simulation tools as an adjunct to experimental work for such problems is of significant interest. Reference [1] shows that the use of computer simulation in this field is increasing, such that improvements in numerical methods and computing power make it possible to address problems of greater complexity and larger scale. Simulation work in this field has applied a number of different numerical methods based on continuum mechanics, particle dynamics, or mixed kinematic schemes. Continuum methods [8] employ either an Eulerian hydrodynamic [9] or a Lagrangian finite element [10] approach, or some arbitrary Lagrangian–Eulerian (ALE)-based generalization of these techniques [11]. A large majority of particle codes employ a smooth particle hydrodynamics technique [12,13]. Some disadvantages of pure continuum-based or pure particle-based methods have motivated the development of mixed continuum–particle formulations [3,14–16]. However, the effective use of existing computer codes in the direct simulation of hypervelocity impacts is limited by the ability to obtain discretization-independent deformation results. During impact loading, large inelastic deformation associated with high strain rates leads, for a broad class of brittle and ductile materials, to degradation and failure by strain localization (i.e., shear bands); therefore, as soon as material failure dominates a deformation process, the material increasingly displays strain-softening, and the finite element computations are considerably affected by the mesh size and alignment when using the classical (local) continuum theories of plasticity and damage. This gives rise to a nonphysical description of the material and structural failure. This can be attributed to the absence of an intrinsic material-length-scale parameter in the constitutive description of the plasticity and damage models, such that this length scale can improve the well-posed nature of the solved (initial) boundary-value problem. Therefore, the objective of this work is to present a novel microdamage constitutive model for high-speed-impact damage problems that possesses several material length scales. This model can be used to produce physically

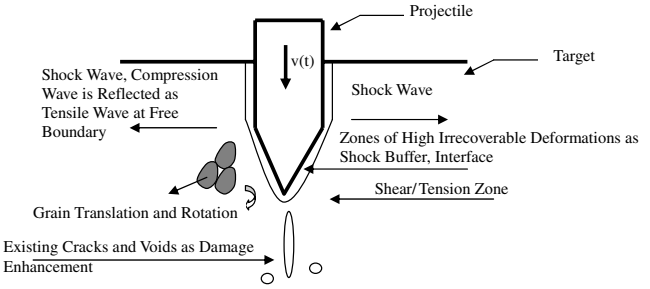

Fig. 1 Phenomenological illustration of the penetration process.

meaningful and numerically converging results within strain localization computations by finite element codes. Moreover, the algorithmic aspects and numerical implementation of this model in finite element codes are presented in this paper.

The key role in the numerical simulation of the impact-damage-related problems is the accurate modeling of the material behavior at high strain rates and temperatures. Many researchers, therefore, have investigated the material failure mechanism during high-velocity-impact conditions with the ultimate goal of developing a micromechanical constitutive model that can effectively simulate the impact damage problem (see, for example, [17–26]). It is noted that none of these constitutive models address the problem of describing high shock compression and subsequent material degradation and failure, in which the latter is expressed as an evolving microflaw having a damage rate determined from micromechanical analysis. Moreover, these models cannot consider the actual sizes, shapes, and orientations of the individual microvoids and microcracks, which may have a predominant influence on the mechanical response of the material. The authors of this work have recently recognized the need for a micromechanical damage model [27–30] that accounts for the nonlocal microscopic interactions between material points (i.e., to take into account the influence of an internal state variable at a point on its neighborhood) in the simulation of metal impact problems. This nonlocal microdamage model is formulated based on the enhanced gradient-dependent theory, which is successful in explaining the size effects encountered at the micron scale and in preserving the well-posed nature of the initial boundary-value problem that governs the solution of material instability triggering strain localization (see Voyiadjis et al. [27,28] and Abu Al-Rub and Voyiadjis [30] for details regarding the use of the gradient theory as a localization limiter, as well as an extensive list of authors who used this approach). Moreover, the viscoplasticity theory (rate dependency) allows the spatial difference operator in the governing equations to retain its ellipticity and, consequently, the initial boundary-value problem is hence well-posed (see, for example, [31–38]). However, the gradient-dependent theories enhance a stronger regularization of the localization problem than the rate-dependent theory. Moreover, the rate-dependent theory cannot explain the size effect of the microdamage zone (i.e., the void/crack size and spacing) on the material failure, whereas the gradient theory can address that.

In this study, a general theoretical framework for the analysis of heterogeneous media that assesses a strong coupling between rate-dependent plasticity and anisotropic rate-dependent damage is presented for high-velocity-impact-related problems. This framework is developed based on thermodynamic laws, nonlinear continuum mechanics, and nonlocal gradient-dependent theory [27–30]. This model uses combined viscosity and nonlocal gradient localization limiters to regularize the dynamic strain localization problem. Material length scales are incorporated explicitly through the nonlocal gradient theory and implicitly through the rate-dependency (viscoplasticity). The proposed formulation includes hypoelastothermoviscoplasticity with anisotropic thermovisco-damage, a dynamic yield criterion, a dynamic damage growth criterion, nonassociated flow rules, thermal softening, nonlinear strain hardening, strain-rate hardening, strain-hardening gradients, strain-rate-hardening gradients, and an equation of state. The idea of bridging length scales is made more general and complete by introducing spatial higher-order gradients in the temporal evolution equations of the internal state variables that describe hardening in coupled viscoplasticity and viscodamage models. The model is mainly developed to regularize the ill-posed problem caused by strain-softening material behavior and to incorporate the size effect (size and spacing of microdefects) in material behavior for high-velocity-impact damage-related problems.

The development of computational algorithms that are consistent with the proposed theoretical formulation is given in detail in this paper. The problem of numerically integrating the constitutive equations in the context of the finite element method is also addressed. The standard return-mapping algorithms of rate-independent problems are extended to rate-dependent problems. Moreover, because the numerical implementation of the gradient-dependent constitutive equations is not a direct task (because of the higher order of the governing equations), a direct and simple computational algorithm for the gradient approach is used. This algorithm can be implemented in the existing finite element codes without numerous modifications, compared with the current numerical approaches for gradient-enhanced models (see Voyiadjis et al. [28]). Furthermore, a trivially incrementally objective integration scheme is established for the rate constitutive relations. The proposed elastic predictor and coupled viscoplastic–viscodamage corrector algorithm allows for total uncoupling of geometrical and material nonlinearities. The nonlinear algebraic system of equations is solved by consistent linearization and the Newton–Raphson iteration. The proposed model is implemented in the explicit finite element code ABAQUS via the user subroutine VUMAT [39]. In this work, complete details are presented for the implementation of the proposed novel numerical algorithms.

Model capabilities are preliminarily illustrated for the dynamic localization of inelastic flow in adiabatic shear bands and compared with the experimental results of Borvik et al. [23] for the perforation of 12-mm-thick Weldox 460E steel plates by deformable blunt projectiles at various impact speeds.

Microdamage Constitutive Model

Generally, three sets of equations are needed to simulate the impact damage problems: a yield criterion (which incorporates the strain rate and temperature effects on the material's strength), an equation of state (which accounts for material pressure sensitivity), and a damage model (which is needed to simulate progressive failure and fracture). The coupled constitutive model of viscoplasticity and ductile viscodamage (rate-dependent damage) used to predict material behavior under dynamic loading conditions (which was earlier derived based on the laws of thermodynamics [27–30]) combines all these requirements. Only the main governing constitutive equations will be given in the following. The model is based on the nonlocal gradient plasticity and gradient damage theories. It includes the nonlocal von Mises yield criterion, the nonassociated flow rules, isotropic and anisotropic strain hardening, strain-rate hardening, softening due to adiabatic heating and anisotropic damage evolution, and a path-dependent equation of state. The stress–strain rate relationship in the spatial and damaged configuration is given by

$$\overset{\nabla}{\boldsymbol{\tau}} = \mathbb{C}:(\boldsymbol{d} - \boldsymbol{d}^{vp} - \boldsymbol{d}^{vd}) - \boldsymbol{A}:\overset{\nabla}{\boldsymbol{\phi}} - \mathbb{C}:\alpha_t \dot{T}\mathbf{1} \tag{1}$$

with

$$\mathbb{C} = \widehat{\boldsymbol{M}}^{-1}:\bar{\mathbb{C}}:\widehat{\boldsymbol{M}}^{-1} \quad \text{and} \quad \widehat{\boldsymbol{M}} = 2[(\mathbf{1} - \widehat{\boldsymbol{\phi}}) \otimes \mathbf{1} + \mathbf{1} \otimes (\mathbf{1} - \widehat{\boldsymbol{\phi}})]^{-1} \tag{2}$$

where ∇ indicates the corotational objective derivative; $\boldsymbol{\tau}$ is the Kirchhoff stress tensor; $\boldsymbol{d}$ is the total rate of deformation; $\boldsymbol{d}^{vp}$ is the viscoplastic rate of deformation; $\boldsymbol{d}^{vd}$ is the viscodamage rate of deformation; $\bar{\mathbb{C}}$ and $\mathbb{C}$ are the fourth-order undamaged and damaged elasticity tensors, respectively; α_t is the thermal expansion

coefficient; $\dot{T}$ is the rate of absolute temperature; and $\mathbf{1}$ is the second-order identity tensor.

The fourth-order tensors $\bar{\mathbb{C}}$ and $\boldsymbol{A}$ are given by the following relations:

$$\begin{aligned}\bar{\mathbb{C}} &= K^e \mathbf{1}\otimes\mathbf{1} + 2G^e I^{\mathrm{dev}} \\ \boldsymbol{A} &= \frac{\partial \widehat{\boldsymbol{M}}^{-1}}{\partial \widehat{\boldsymbol{\phi}}} : \widehat{\boldsymbol{M}} : \boldsymbol{\tau} + \mathbb{C} : \widehat{\boldsymbol{M}} : \frac{\partial \widehat{\boldsymbol{M}}^{-1}}{\partial \widehat{\boldsymbol{\phi}}} : \bar{\mathbb{C}}^{-1} : [\boldsymbol{\tau} + \alpha_t (T - T_r)\mathbf{1}]\end{aligned} \tag{3}$$

where K^e is the bulk modulus, G^e is the shear modulus, T_r is the reference temperature, and $\mathbf{I}^{dev}$ is the deviatoric part of the fourth-order identity tensor $\mathbf{I}$. In the undamaged configuration, Eq. (1) can be written as follows:

$$\overset{\triangledown}{\bar{\boldsymbol{\tau}}} = \bar{\mathbb{C}} : (\bar{\boldsymbol{d}} - \bar{\boldsymbol{d}}^{vp}) - \alpha_t \dot{T}\mathbf{1} \tag{4}$$

Note that hereafter, (:) stands for tensor contraction, the superimposed dot $(\cdot)$ indicates the differentiation with respect to time t, the superimposed hat indicates a nonlocal quantity, the superimposed dash indicates a quantity in the undamaged (effective) configuration, and $\otimes$ denotes the dyadic product.

Materials with microstructure are nonlocal in behavior, due to the interplay of characteristic lengths, including the sizes or spacing of defect clusters (e.g., microcracks, microvoids, and dislocations). Because traditional continuum mechanics does not contain characteristic lengths, the use of the nonlocal concept is required to incorporate a microstructural length scale that introduces long-range microstructural interactions in which the stress response at a material point is assumed to depend on the state of its neighborhood in addition to the state of the material point itself. Moreover, this length scale preserves the well-posed nature of the initial boundary-value problem governing the solution of material instability triggering strain localization. In the following, the nonlocality is incorporated through the use the gradient-dependent theory, such that if $\boldsymbol{\phi}$ is some "local" field in a domain V, the corresponding nonlocal field $\widehat{\phi}$ is defined as follows:

$$\widehat{\boldsymbol{\phi}} = \boldsymbol{\phi} + \tfrac{1}{2}\ell^2 \nabla^2 \boldsymbol{\phi} \tag{5}$$

where ℓ is the *internal material length scale*, which weights each component of the gradient term identically, and ∇^2 is the Laplacian operator. The length scale ℓ should be obtained from gradient-dominant experiments such as indentation tests, bending tests, or torsion tests [40–42]. The role of the material length scale in solving the impact damage problem and in preserving the objectivity of the continuum modeling and numerical simulation of the localization problem is the main concern of this paper. The first-order gradients are disregarded because the isotropic nonlocal influence is assumed.

The viscoplastic rate of deformation $\boldsymbol{d}^{vp}$, the viscodamage rate of deformation $\boldsymbol{d}^{vd}$, the rate of the second-order damage tensor $\boldsymbol{\phi}$, and the viscoplastic rate of deformation in the undamaged configuration $\bar{\boldsymbol{d}}^{vp}$ are given as follows:

$$\begin{aligned}\boldsymbol{d}^{vp} &= \dot{\lambda}^{vp}\frac{\partial f}{\partial \boldsymbol{\tau}}, \qquad \boldsymbol{d}^{vd} = \dot{\lambda}^{vd}\frac{\partial g}{\partial \boldsymbol{\tau}} \\ \overset{\triangledown}{\boldsymbol{\phi}} &= \dot{\lambda}^{vp}\frac{\partial f}{\partial \boldsymbol{Y}} + \dot{\lambda}^{vd}\frac{\partial g}{\partial \boldsymbol{Y}}, \qquad \bar{\boldsymbol{d}}^{vp} = \dot{\lambda}^{vp}\frac{\partial f}{\partial \bar{\boldsymbol{\tau}}}\end{aligned} \tag{6}$$

where the potentials f and g are the nonlocal viscoplastic and viscodamage conditions given in the undamaged (effective) configuration, respectively, by

$$\begin{aligned}f = \sqrt{\tfrac{3}{2}(\bar{\boldsymbol{\tau}}' - \widehat{\bar{\boldsymbol{X}}}) : (\bar{\boldsymbol{\tau}}' - \widehat{\bar{\boldsymbol{X}}})} - [\bar{Y}_{yp} + \widehat{\bar{\boldsymbol{R}}}(\bar{\widehat{p}})][1 + (\eta^v \dot{\bar{\widehat{p}}})^{1/m}] \\ \times [1 - (T/T_m)^n] \le 0\end{aligned} \tag{7}$$

$$\begin{aligned}g = \sqrt{(\widehat{\boldsymbol{Y}} - \widehat{\boldsymbol{H}}) : (\widehat{\boldsymbol{Y}} - \widehat{\boldsymbol{H}})} - [r_o + \widehat{K}(\widehat{r})][1 + (\eta^v \dot{\bar{\widehat{p}}})^{1/m}] \\ \times [1 - (T/T_m)^n] \le 0\end{aligned} \tag{8}$$

where $\bar{\boldsymbol{\tau}}'$ is the effective deviatoric stress tensor; $\bar{Y}_{yp}$ is the initial yield strength (at zero absolute temperature, zero plastic strain, and static strain rate); $\bar{\widehat{R}}(\bar{\widehat{p}})$ is the nonlocal isotropic hardening function, $\bar{\widehat{\boldsymbol{X}}}$ is the nonlocal anisotropic (kinematic) hardening stress;

$$\bar{p} = \int_0^t \sqrt{\frac{2}{3}\bar{\boldsymbol{d}}_{ij}^{vp}\bar{\boldsymbol{d}}_{ij}^{vp}}\, dt$$

is the effective accumulative viscoplastic strain; m and n are material constants; η^v is the relaxation time; the nonlocal damage forces $\widehat{\boldsymbol{Y}}$ and $\widehat{K}(\widehat{r})$ are, respectively, characterizing the energy release rate and the damage isotropic hardening function; r_o is the initial damage threshold; $\widehat{r} = \sqrt{\widehat{\boldsymbol{\phi}} : \widehat{\boldsymbol{\phi}}}$ is the nonlocal damage accumulation; and T_m is the melting temperature.

The viscoplastic and viscodamage multipliers $\dot{\lambda}^{vp}$ and $\dot{\lambda}^{vd}$ can be obtained in a nonlocal sense using the following generalized Kuhn–Tucker conditions for rate-dependent problems:

$$\begin{aligned}&\dot{\lambda}^{vp} \ge 0, \qquad f \le 0 \Leftrightarrow \dot{\lambda}^{vp} f = 0 \quad \text{and} \quad \dot{\lambda}^{vd} \ge 0, \\ &g \le 0 \Leftrightarrow \dot{\lambda}^{vd} g = 0\end{aligned} \tag{9}$$

The nonlocal evolution equations for the isotropic and kinematic hardening in the undamaged configuration are given by

$$\dot{\bar{\widehat{R}}} = \dot{\bar{R}} + \frac{1}{2}\ell^2 \nabla^2 \dot{\bar{R}} \quad \text{with} \quad \dot{\bar{R}} = \frac{a_1 \dot{\lambda}^{vp}}{(1 - \widehat{r})^2}(1 - k_1 \bar{\widehat{R}}) \tag{10}$$

and

$$\overset{\triangledown}{\bar{\widehat{\boldsymbol{X}}}} = \overset{\triangledown}{\bar{\boldsymbol{X}}} + \frac{1}{2}\ell^2 \nabla^2 \overset{\triangledown}{\bar{\boldsymbol{X}}} \quad \text{with} \quad \overset{\triangledown}{\bar{\boldsymbol{X}}}_{ij} = \widehat{\boldsymbol{M}} : \widehat{\boldsymbol{M}} : \left(\frac{\partial f}{\partial \bar{\boldsymbol{\tau}}} - k_2 \bar{\widehat{\boldsymbol{X}}}\right) \tag{11}$$

The evolution equations for the nonlocal viscodamage isotropic and kinematic hardening functions are given by

$$\dot{\widehat{K}} = \dot{K} + \tfrac{1}{2}\ell^2 \nabla^2 \dot{K} \quad \text{with} \quad \dot{K} = a_3 \dot{\lambda}^{vd}(1 - h_1 \widehat{K}) \tag{12}$$

and

$$\overset{\triangledown}{\widehat{\boldsymbol{H}}} = \overset{\triangledown}{\boldsymbol{H}} + \frac{1}{2}\ell^2 \nabla^2 \overset{\triangledown}{\boldsymbol{H}} \quad \text{with} \quad \overset{\triangledown}{\boldsymbol{H}} = a_4 \dot{\lambda}^{vd}\left(\frac{\partial g}{\partial \boldsymbol{Y}} - h_2 \widehat{\boldsymbol{H}}\right) \tag{13}$$

The nonlocal strain energy release rate is given by

$$\widehat{\boldsymbol{Y}} = \frac{1}{2}[\boldsymbol{\tau} - \alpha_t (T - T_r)\mathbf{1}] : \widehat{\boldsymbol{M}} : \frac{\partial \widehat{\boldsymbol{M}}^{-1}}{\partial \widehat{\boldsymbol{\phi}}} : \mathbb{C}^{-1} : [\boldsymbol{\tau} + \alpha_t (T - T_r)\mathbf{1}] \tag{14}$$

where k_i, h_i, and a_i $(i = 1\text{–}4)$ are material constants that can be identified from conventional tests (e.g., uniaxial tension test).

The thermodynamic pressure stress P for a shock compressed solid is given as follows:

$$\begin{aligned}P = (1 - \gamma) c_v T^{ig} \varepsilon^e \quad \text{with} \quad T^{ig} = T_r \exp[(\eta - \eta_r)/c_v][1 + \varepsilon^e]^{(\gamma - 1)} \\ \times \exp\{(\gamma - 1)[1/(1 + \varepsilon^e) - 1]\}\end{aligned} \tag{15}$$

which gives the equation of state necessary for high-impact loading. The equation of state accounts for compressibility effects (changes in density) and irreversible thermodynamic processes. The parameter $\gamma = c_p/c_v$ is the ratio of the specific heats, where c_p and c_v are the specific heats at constant pressure and constant volume, respectively; $\varepsilon^e = 1/J^e - 1$ is the nominal elastic volumetric strain, where $J^e = \det(\boldsymbol{F}^e)$ is the determinate of elastic deformation gradient $\boldsymbol{F}^e$; T^{ig} is chosen to have the form of ideal gas temperature; and η is the entropy,

which is expressed by

$$\eta = \eta_r + \frac{3}{\rho_o} K^e \alpha_t \boldsymbol{e}^e : \mathbf{1} + c_p (T - T_r) \tag{16}$$

In the preceding relation, η_r is the reference entropy, ρ_o is the reference density, and $\boldsymbol{e}^e$ is the Eulerian elastic strain tensor.

To establish the actual heat generation that occurs during the highly transient impact events of the thermomechanically coupled finite element, the development of a heat equation is imperative. However, because the whole impact process lasts a few hundredths of a μs, the effect of heat conduction is negligible over the domain of the specimen; therefore, an adiabatic condition is assumed, such that the increase in temperature is calculated by the following heat equation:

$$\rho_o c_p \dot{T} = \Upsilon \boldsymbol{\tau}' : (\boldsymbol{d}^{vp} + \boldsymbol{d}^{vd}) + J^e P (\boldsymbol{d}^e : \mathbf{1}) \tag{17}$$

where Υ is the heat fraction characterizing the fraction of heat dissipated during plastic and damage works.

In this development, one bases the failure criterion on the nonlocal evolution of the accumulated microdamage internal state variable $\widehat{\boldsymbol{\phi}}$ and the equation of state for the thermodynamic pressure. It implies that for

$$\|\widehat{\phi}\| = \sqrt{\widehat{\phi}_{ij}\widehat{\phi}_{ij}} \geq \|\phi\|_c \quad \text{and/or} \quad P \geq P_{\text{cutoff}} \tag{18}$$

the material loses its carrying capacity, where $\|\phi\|_c$ is the critical damage when catastrophic failure in the material takes place, and P_{cutoff} is the pressure cutoff value when tensile failure or compressive failure occurs.

Many authors tend to use a constant value for the length-scale parameter and neglect its variation with the state of loading. For example, the damage zone ahead of the crack tip or the mean dislocation spacing will decrease with increasing strain rate and increase with decreasing temperature (which, for small-scale yielding, is of the order of microns. This causes the intrinsic material length scale to decrease with increasing strain rates and to increase with temperature decrease [40,42]. However, opposite behavior is anticipated for the gradient term; that is, gradients are inversely proportional to the length scale over which plastic and/or damage deformations occur. Therefore, the strain-rate effect and temperature variation are crucial to the reliability of the proposed length-scale parameters. Particularly, in dynamic problems, their inclusion becomes more necessary. To the authors' best knowledge, very limited numerical investigations and experimental studies have been carried out that incorporate the influence of strain-rate and temperature variation on the gradient plasticity and damage, or more specifically, on the size effect. Motivated by this crucial observation, Abu Al-Rub and Voyiadjis [40] formulated the following evolution equation for the length-scale parameter based on dislocation mechanics of metallic materials, such that

$$\dot{\ell} = \ell \nu_o \exp[-(U_o/kT)\{1 - (\sigma^*/\sigma_o^*)^p\}^q] \tag{19}$$

where ν_o is the fundamental vibration frequency of the dislocation, p and q are material constants, k is Boltzmann's constant, U_o is the referential activation energy, σ^* is the thermal stress, and σ_o^* is the reference thermal stress.

Numerical Aspects

In this section, the numerical integration of the nonlocal geometrically nonlinear thermoviscoinelastic model presented in the previous section is developed. Let $t_o, t_1, \ldots, t_n$ and $t_{n+1} = t_n + \Delta t, \ldots$ be convenient time instances along the time interval over which the dynamic response of the body is sought. Consider the time step $\Delta t = t_{n+1} - t_n$ at $t = t_n$ where all quantities are known, which are the converged values of the previous step, and the solution must be computed at t_{n+1} for a given body load increment Δb and surface load increment Δt.

Let the dynamic evolution of a hypoelastic–thermoviscoplastic and thermoviscodamaged body of volume V and surface S be governed at step time $n+1$, by the constitutive relations presented in the previous section, and by the following momentum, initial, and compatibility relations:

$$\boldsymbol{L}^T \boldsymbol{\tau}_{n+1} + \rho_o \boldsymbol{b}_{n+1} = \rho_o \dot{\boldsymbol{v}}_{n+1} \quad \text{in } V; \qquad \boldsymbol{t}_{n+1} = \boldsymbol{\tau}_{n+1} \boldsymbol{n} \quad \text{on } S_t \tag{20}$$

$$\boldsymbol{u} = \boldsymbol{u}_o, \qquad \boldsymbol{v} = \boldsymbol{v}_o \quad \text{at } t = t_o \tag{21}$$

$$\boldsymbol{l}_{n+1} = \nabla \boldsymbol{v}_{n+1} = \boldsymbol{C} \boldsymbol{v}_{n+1} \quad \text{in } V \tag{22}$$

$$\boldsymbol{u}_{n+1} = \tilde{\boldsymbol{u}} \quad \text{on } S_u; \qquad \boldsymbol{v}_{n+1} = \tilde{\boldsymbol{v}} \quad \text{on } S_v; \qquad T_{n+1} = \tilde{T} \quad \text{on } S_T \tag{23}$$

where $(\bullet)_{n+1} = (\bullet)_n + \Delta(\bullet)$ is the additive decomposition of each of the internal variables. For algorithmic convenience, the authors have shifted to matrix vector notation in this section. Equations (20) express the discrete dynamic motion in the volume V and equilibrium on the free part of the boundary S_t at $n+1$. Viscohypoelasticity is not considered in this study; viscous damping effects are neglected. $\boldsymbol{L}$ is the differential operator; $\boldsymbol{b}$ and $\boldsymbol{t}$ are the body force and the surface traction vectors, respectively; $\boldsymbol{u}$ is the three-component displacement vector; and $\boldsymbol{n}$ denotes the outward normal to the surface S. The initial conditions on displacements and velocities are given by Eqs. (21). Compatibility relation in volume V is given by Eq. (22). The boundaries S_u, S_v, and S_T are parts of the boundary in which the displacement $\tilde{\boldsymbol{u}}$, the velocity $\tilde{\boldsymbol{v}}$, and the temperature $\tilde{T}$ is prescribed, respectively. It is clear that $S_t \cup S_u \cup S_v \cup S_T = S$ and $S_t \cap S_u = 0$.

In the context of the finite element method, the discrete problem can be obtained via a spatial displacement-based projection of the semidiscrete (i.e., discrete in space and continuous in time) problem into a finite dimensional subspace of admissible continuous shape functions. Consequently, in the following sections, the procedure for solving the derived set of governing equations using the finite element method is described thoroughly. To integrate the set of constitutive equations, a return-mapping algorithm is developed in the subsequent sections.

Return-Mapping Algorithm

Considering a given configuration of known set of positions $\boldsymbol{X}$ at time t_n, the problem is now to update all state variables to a new configuration defined by its respective set of positions $\boldsymbol{x}$ (which are supposed to be known) at time t_{n+1}. This situation typically arises in a nonlinear finite element problem in which the new positions x are determined from the discretized version of the momentum equation (20).

In this section, a semi-implicit stress-integration algorithm for rate-dependent problems [43] is recalled. This stress update algorithm treats the rate-independent and rate-dependent problems in a unified way. It is unified in a sense that the same routines are able to integrate both rate-independent and rate-dependent models by simply setting the viscosity parameter η^v in Eqs. (7) and (8) to zero. Moreover, in this paper, this algorithm is extended to fully nonlocal coupled viscoplastic–viscodamage constitutive equations with a two-step predictor-corrector structure: hypoelastic predictor and coupled viscoplastic–viscodamage corrector [44]. In the model presented in this paper, there exists two coupled surfaces, f and g, and for each iteration, f and g should be corrected simultaneously (see Fig. 2). The different steps of the integration algorithm are detailed next.

If the variables at iteration i, such as $\boldsymbol{\tau}_i$, $\widehat{\boldsymbol{X}}_i$, $\widehat{\boldsymbol{R}}_i$, $\widehat{\boldsymbol{\phi}}_i$, $\widehat{\boldsymbol{H}}_i$, $\widehat{K}_i$, $\widehat{\boldsymbol{Y}}_i$, and T_i are assumed to be determined and the values of $\boldsymbol{d}$ and Δt are given, then $\boldsymbol{\tau}_{i+1}$, which satisfies the discretized constitutive equations, can be obtained. In the following, a hypoelastic predictor and coupled

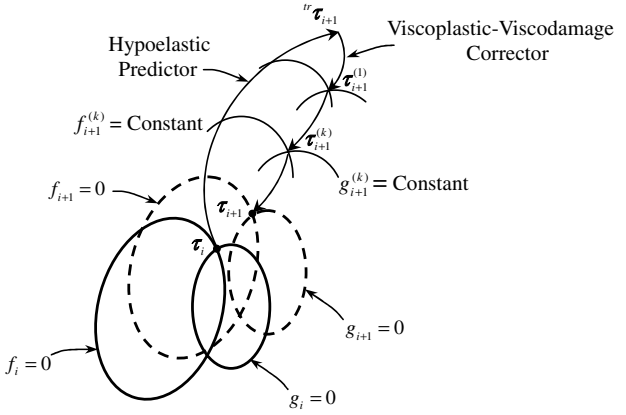

Fig. 2 Conceptual representation of the hypoelastic predictor and coupled viscoplastic–viscodamage corrector algorithm.

viscoplastic–viscodamage corrector is proposed. In the first step, the hypoelastic predictor problem is solved with initial conditions that are the converged values of the previous iteration i, while keeping the irreversible variables frozen. This produces a trial stress state ${}^{tr}\boldsymbol{\tau}$, which, if outside the viscoplastic surface f and the viscodamage surface g, is taken as the initial conditions for the solution of the viscoplastic–viscodamage corrector problem. The scope of this second step is to restore the generalized consistency condition by returning the trial stress to the viscoplastic surface f and the viscodamage surface g simultaneously, as conceptually represented in Fig. 2.

However, one of the major challenges when integrating the constitutive equations in finite deformation context is to achieve the incremental objectivity (i.e., to maintain correct rotational transformation properties all along a finite time step). A procedure that has now become very popular is to first rewrite the constitutive equations in a corotational moving frame. Therefore, Voyiadjis et al. [43] showed that by assuming that the variables of the model at iteration i and the displacement field $\boldsymbol{u} = \boldsymbol{x}_{i+1} - \boldsymbol{x}_i$ at iteration $i+1$ are known, the trial elastic stress can then be given in the corotational frame by

$$ {}^{tr}\boldsymbol{\tau}_{i+1} = \boldsymbol{R}(\boldsymbol{\tau}_i + \mathbb{C}_i{:}\boldsymbol{E})\boldsymbol{R}^T \tag{24} $$

where $\boldsymbol{R}$ is the polar decomposition ($\boldsymbol{F} = \boldsymbol{R}\cdot\boldsymbol{U}$) rotation matrix and $\boldsymbol{E}$ is the (incremental) logarithmic strain tensor between the reference configuration and the current one, which is given by

$$ \boldsymbol{E} = \ell_n \boldsymbol{U} = \tfrac{1}{2}\ell_n \boldsymbol{U}^2 = \tfrac{1}{2}\ell_n(\boldsymbol{F}^T\boldsymbol{F}) \tag{25} $$

where $\boldsymbol{F}$ is the total deformation gradient and $\boldsymbol{U}$ is the right stretch tensor.

In the preceding procedure, it is essential to realize that $\boldsymbol{F} = \boldsymbol{R}\cdot\boldsymbol{U}$ are incremental tensors; in the case of rigid body motion, $\ell_n \boldsymbol{U} = 0$, thus the stress tensor will be exactly updated by the relation $\boldsymbol{\tau}_{n+1} = \boldsymbol{R}\boldsymbol{\tau}_n\boldsymbol{R}^T$, whatever the amplitude of the rotation. The rotation tensor $\boldsymbol{R}$ is directly and exactly computed from the polar decomposition and $\boldsymbol{R}$ only needs to be evaluated once per time step. All kinematic quantities are based on the deformation gradient $\boldsymbol{F}$ over the considered time step, a quantity that is readily available in nonlinear finite element codes.

Coupled Viscoplastic–Viscodamage Corrector

If $f({}^{tr}\boldsymbol{\tau}_{i+1}, \widehat{\boldsymbol{X}}_i, \widehat{R}_i, \dot{\widehat{p}}_i, T_i, \widehat{\boldsymbol{\phi}}_i) \le 0$ and $g({}^{tr}\widehat{\boldsymbol{Y}}_{i+1}, \widehat{\boldsymbol{H}}_i, \widehat{K}_i, \dot{\widehat{p}}_i, T_i, \widehat{\boldsymbol{\phi}}_i) \le 0$, the process is clearly undamaged elastic and the trial stress is, in fact, the final state. On the other hand, if $f > 0$ and $g > 0$, the Kuhn–Tucker loading/unloading conditions (9) are violated by the trial stress that now lies outside f and g (see Fig. 2). Consistency is restored by a generalization of the classical return-mapping algorithm to rate-dependent problems [43]. Because the objective rates reduce to a simple time derivative due to the fact that the global configuration is held fixed, the coupled viscoplastic–viscodamage corrector problem may then be rephrased as

$$ \dot{\boldsymbol{\tau}} = -\mathbb{C}{:}(\boldsymbol{d}^{vp} + \boldsymbol{d}^{vd}) - \boldsymbol{A}{:}\dot{\boldsymbol{\phi}} - \mathbb{C}{:}\alpha_t\dot{T}\boldsymbol{1} \tag{26} $$

The hypoelastic predictor and coupled viscoplastic–viscodamage corrector step yields the final stress as

$$ \boldsymbol{\tau}_{i+1} = {}^{tr}\boldsymbol{\tau}_{i+1} - \mathbb{C}_i{:}(\boldsymbol{d}^{vp} + \boldsymbol{d}^{vd}) - \boldsymbol{A}_i{:}\dot{\boldsymbol{\phi}} - \mathbb{C}_i{:}\alpha_t\dot{T}\boldsymbol{1} \tag{27} $$

where $\dot{T}$ is calculated from the heat-balance equation (17), whereas $\dot{\lambda}^{vp}$ and $\dot{\lambda}^{vd}$ are calculated using the nonlocal computational algorithm presented in [45,46]. In the following sequence, $\dot{\lambda}^{vp}$ and $\dot{\lambda}^{vd}$ that appear in Eqs. (6) are calculated using the nonlocal computational algorithm in [45] through the adiabatic heating condition (17), the generalized viscoplastic consistency condition (7), and the generalized viscodamage consistency condition (8).

By making use of the evolution equations for $\boldsymbol{d}^{vp}$ and $\boldsymbol{d}^{vd}$ from Eqs. (6), respectively, into the adiabatic heat equation (17), the temperature evolution can then be reduced to

$$ \dot{T} = \frac{1}{\rho_o c_p} J^e \boldsymbol{P}\boldsymbol{1}{:}\boldsymbol{d} + Q_1^{tp}\dot{\lambda}^{vp} + Q_1^{td}\dot{\lambda}^{vd} \tag{28} $$

where Q_1^{tp} and Q_1^{td} are obtained from the previous iteration i and are given by

$$ Q_1^{tp} = \frac{1}{\rho_o c_p}\Upsilon\boldsymbol{\tau}'{:}\frac{\partial f}{\partial \boldsymbol{\tau}}, \qquad Q_1^{td} = \frac{1}{\rho_o c_p}\Upsilon\boldsymbol{\tau}'{:}\frac{\partial f}{\partial \boldsymbol{Y}} \tag{29} $$

Moreover, one requires the satisfaction of the generalized viscoplasticity consistency condition $\dot{f}$ [Eq. (7)] at the end of iteration $i+1$, such that

$$ \frac{\partial f}{\partial \bar{\boldsymbol{\tau}}}{:}\overset{\nabla}{\bar{\boldsymbol{\tau}}} + \frac{\partial f}{\partial \bar{\boldsymbol{X}}}{:}\overset{\nabla}{\bar{\boldsymbol{X}}} + \frac{\partial f}{\partial \bar{R}}\dot{\bar{R}} + \frac{1}{\Delta t}\frac{\partial f}{\partial \dot{\bar{p}}}\dot{\bar{p}} + \frac{\partial f}{\partial T}\dot{T} = 0 \tag{30} $$

Because the local iteration process is applied within the time step $t + \Delta t$ (i.e., at step $n+1$) and the updated Lagrangian formulation is used, then $\dot{\bar{p}} = \ddot{\bar{p}}\Delta t$ is used in obtaining Eq. (30). Substitution of the stress-rate equation $\overset{\nabla}{\bar{\boldsymbol{\tau}}}$ from Eqs. (4), (10), (11), and (28) and into Eq. (30) yields the following expression:

$$ \left(\frac{\partial f}{\partial \boldsymbol{\tau}}{:}\boldsymbol{C} + \boldsymbol{Z}^p\right){:}\boldsymbol{d} + Q_1^p\dot{\lambda}^{vp} + Q_2^p\nabla^2\dot{\lambda}^{vp} + Q_3^p\dot{\lambda}^{vd} + Q_4^p\nabla^2\dot{\lambda}^{vd} = 0 \tag{31} $$

where $\boldsymbol{Z}^p$ and Q_k^p ($k = 1,\ldots,4$) are obtained from the previous i iteration and are given by

$$ \boldsymbol{Z}^p = -\frac{\partial f}{\partial T}\cdot(J^e P + T\alpha_t)\boldsymbol{1} \tag{32} $$

$$ \begin{aligned} Q_1^p = Q_1^{tp} &- \frac{\partial f}{\partial \boldsymbol{\tau}}{:}\left(\boldsymbol{C}{:}\frac{\partial f}{\partial \boldsymbol{\tau}} + \boldsymbol{A}{:}\frac{\partial f}{\partial \boldsymbol{Y}}\right) + \left[\frac{\partial f}{\partial p} + \frac{1}{\Delta t}\frac{\partial f}{\partial \dot{p}}\right]\frac{(1 - k_1\bar{\widehat{\boldsymbol{R}}})}{1 - \widehat{r}} \\ &+ \left[\frac{\partial f}{\partial \nabla^2 p} + \frac{1}{\Delta t}\frac{\partial f}{\partial \nabla^2 \dot{p}}\right]\left[\frac{\nabla^2 r}{(1-\widehat{r})^2}(1 - k_1\bar{\widehat{R}}) - \frac{k_1}{1-\widehat{r}}\nabla^2\bar{R}\right] \\ &- \frac{1}{a_2}\frac{\partial f}{\partial \bar{\boldsymbol{X}}}{:}\widehat{\boldsymbol{M}}{:}\left(\frac{\partial f}{\partial \bar{\boldsymbol{X}}} + k_2\bar{\widehat{\boldsymbol{X}}}\right) - \frac{2}{a_2\ell^2}\frac{\partial f}{\partial \nabla^2\bar{\boldsymbol{X}}}{:}\left[\nabla^2\widehat{\boldsymbol{M}}{:}\left(\frac{\partial f}{\partial \bar{\boldsymbol{X}}} + k_2\bar{\widehat{\boldsymbol{X}}}\right)\right. \\ &\left. + k_2\widehat{\boldsymbol{M}}{:}\nabla^2\bar{\boldsymbol{X}}\right] + \frac{\partial f}{\partial \boldsymbol{\phi}}{:}\frac{\partial f}{\partial \boldsymbol{Y}} \end{aligned} \tag{33} $$

$$Q_2^p = \left[\frac{\partial f}{\partial \nabla^2 p} + \frac{1}{\Delta t}\frac{\partial f}{\partial \nabla^2 \dot{p}}\right]\frac{(1-k_1\bar{\widehat{R}})}{1-\bar{r}} - \frac{2}{a_2\ell^2}\frac{\partial f}{\partial \nabla^2 \bar{\boldsymbol{X}}}:\widehat{\boldsymbol{M}}:\left(\frac{\partial f}{\partial \bar{\boldsymbol{X}}} + k_2\bar{\widehat{\boldsymbol{X}}}\right) + \frac{\partial f}{\partial \nabla^2 \boldsymbol{\phi}}:\frac{\partial f}{\partial \boldsymbol{Y}} \tag{34}$$

$$Q_3^p = Q_1^{td} - \frac{\partial f}{\partial \boldsymbol{\tau}}:\left(\boldsymbol{C}:\frac{\partial g}{\partial \boldsymbol{\tau}} + \boldsymbol{A}:\frac{\partial g}{\partial \boldsymbol{Y}}\right) + \frac{\partial f}{\partial \boldsymbol{\phi}}:\frac{\partial g}{\partial \boldsymbol{Y}} \tag{35}$$

$$Q_4^p = \frac{\partial f}{\partial \nabla^2 \boldsymbol{\phi}}:\frac{\partial g}{\partial \boldsymbol{Y}} \tag{36}$$

Similarly, the generalized viscodamage consistency condition $\dot{g}$ [Eq. (8)] needs to be satisfied. Because the viscodamage driving force $\widehat{\boldsymbol{Y}}$ is a function of $\boldsymbol{\tau}$ and $\widehat{\boldsymbol{\phi}}$, one can then express $\dot{g}$ as follows:

$$\dot{g} \equiv \frac{\partial g}{\partial \boldsymbol{\tau}}:\overset{\triangledown}{\boldsymbol{\tau}} + \frac{\partial g}{\partial \widehat{\boldsymbol{\phi}}}\overset{\triangledown}{\widehat{\boldsymbol{\phi}}} + \frac{\partial g}{\partial \widehat{\boldsymbol{H}}}\overset{\triangledown}{\widehat{\boldsymbol{H}}} + \frac{\partial g}{\partial \widehat{K}}\dot{\widehat{K}} + \frac{1}{\Delta t}\frac{\partial f}{\partial \dot{\bar{p}}}\dot{\bar{p}} + \frac{\partial g}{\partial T}\dot{T} = 0 \tag{37}$$

Substitution of the stress-rate equation $\overset{\triangledown}{\boldsymbol{\tau}}$ from Eq. (1) along with Eqs. (6), (12), (13), and (28) and into Eq. (37) yields the following expression:

$$\left(\frac{\partial g}{\partial \boldsymbol{\tau}}:\boldsymbol{C} + \boldsymbol{Z}^d\right):\boldsymbol{d} + Q_1^d\dot{\lambda}^{vp} + Q_2^d\nabla^2\dot{\lambda}^{vp} + Q_3^d\dot{\lambda}^{vd} + Q_4^d\nabla^2\dot{\lambda}^{vd} = 0 \tag{38}$$

where $\boldsymbol{Z}^d$ and Q_k^d $(k = 1, \ldots, 4)$ are obtained from the previous i iteration and are given by

$$\boldsymbol{Z}^d = -\left(\frac{\partial g}{\partial T} - \frac{\partial g}{\partial \boldsymbol{\tau}}:\alpha_t\mathbf{1}\right)\cdot(J^e P + T\alpha_t)\mathbf{1} \tag{39}$$

$$Q_1^d = Q_1^{tp} - \frac{\partial g}{\partial \boldsymbol{\tau}}:\left(\boldsymbol{C}:\frac{\partial f}{\partial \boldsymbol{\tau}} + \boldsymbol{A}:\frac{\partial f}{\partial \boldsymbol{Y}}\right) + \frac{\partial g}{\partial \boldsymbol{\phi}}:\frac{\partial f}{\partial \boldsymbol{Y}} \tag{40}$$

$$Q_2^d = \frac{\partial g}{\partial \nabla^2 \boldsymbol{\phi}}:\frac{\partial f}{\partial \boldsymbol{Y}} \tag{41}$$

$$Q_3^d = Q_1^{tp} - \frac{\partial g}{\partial \boldsymbol{\tau}}:\left(\boldsymbol{C}:\frac{\partial g}{\partial \boldsymbol{\tau}} + \boldsymbol{A}:\frac{\partial g}{\partial \boldsymbol{Y}}\right) + \frac{\partial g}{\partial r}(1-h_1\widehat{K}) - \frac{2h_1}{a_3\ell^2}\frac{\partial g}{\partial \nabla^2 r}\nabla^2 K + \frac{1}{\Delta t}\frac{\partial g}{\partial \dot{\bar{p}}} - \frac{1}{a_4}\frac{\partial g}{\partial \boldsymbol{H}}:\left(\frac{\partial g}{\partial \boldsymbol{H}} + h_2\widehat{\boldsymbol{H}}\right) - \frac{2h_2}{a_4\ell^2}\frac{\partial g}{\partial \nabla^2 \boldsymbol{H}}:\nabla^2\boldsymbol{H}\frac{\partial g}{\partial \boldsymbol{\phi}}:\frac{\partial g}{\partial \boldsymbol{Y}} \tag{42}$$

$$Q_4^d = \frac{\partial g}{\partial \nabla^2 r}(1-h_1\widehat{K}) - \frac{1}{\Delta t}\frac{\partial g}{\partial \nabla^2 \dot{\bar{p}}} - \frac{2h_2}{a_4\ell^2}\frac{\partial g}{\partial \nabla^2 \boldsymbol{H}}\left(\frac{\partial g}{\partial \boldsymbol{H}} + h_2\widehat{\boldsymbol{H}}\right) + \frac{\partial g}{\partial \nabla^2 \boldsymbol{\phi}}\Big|^T\frac{\partial g}{\partial \boldsymbol{Y}} \tag{43}$$

Because of the higher order of the governing equations (31) and (38) in the inelastic region, considerable difficulties are experienced with their numerical implementation. The consistency condition of inelasticity is no longer an algebraic equation but is a differential one because of $\nabla^2\dot{\lambda}^{vp}$ and $\nabla^2\dot{\lambda}^{vd}$, which needs to be calculated along with

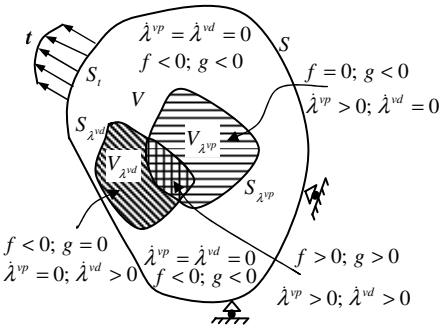

Fig. 3 Schematic representation of elastic, viscoplastic, and viscodamage boundaries.

$\dot{\lambda}^{vp}$ and $\dot{\lambda}^{vd}$. Another complication is the higher-order boundary conditions that are necessary from the mathematical point of view and have to be prescribed on the moving elastoinelastic boundary (Fig. 3). These internal boundaries are not always easy to interpret physically. In the following, the robust numerical technique that was developed in [45,46] is used to calculate the Laplacian terms $\nabla^2\dot{\lambda}^{vp}$ and $\nabla^2\dot{\lambda}^{vd}$.

Computation of the Laplacian of Viscoplasticity and Viscodamage Multipliers

In the approach proposed by Abu Al-Rub and Voyiadjis [45], which is extended to finite strain inelasticity by Voyiadjis and Abu Al-Rub [46], the nonlocal consistency condition is transformed into a linear set of equations that depends on the material parameters and on the current coordinates of the integration points. These sets of linear equations are solved by any numerical iterative method for the inelastic multipliers $\dot{\lambda}^{vp}$ and $\dot{\lambda}^{vd}$ at the integration points that exist in a global (nonlocal) superelement of eight adjacent local elements in a nonlocal sense (Fig. 4). The gradient terms $\nabla^2\dot{\lambda}^{vp}$ and $\nabla^2\dot{\lambda}^{vd}$ at each integration point in the local element are evaluated from the derivatives of a polynomial that interpolates the value of the inelastic multipliers $\dot{\lambda}^{vp}$ and $\dot{\lambda}^{vd}$ in the superelement with classical integration points. In addition, this procedure enforces the generalized consistency conditions $\dot{f}$ and $\dot{g}$ in the sense of distributions (i.e., f and g are satisfied at the end of the loading step). However, in this approach, there in no need to consider the inelastic multipliers as additional degrees of freedom. Therefore, by using this approach, one does not need to introduce high-order continuous shape functions (e.g., C^1 class or penalty-enhanced C^o class functions) for the interpolation of the multiplier fields in the finite element context, as is usually adopted for the gradient-dependent models (see, for example, [28,47,48]). In consequence, a straightforward one-field C^o-continuous finite element implementation can be easily used. Furthermore, this algorithm has the major advantage that it avoids boundary conditions on the moving elastoinelastic boundary,

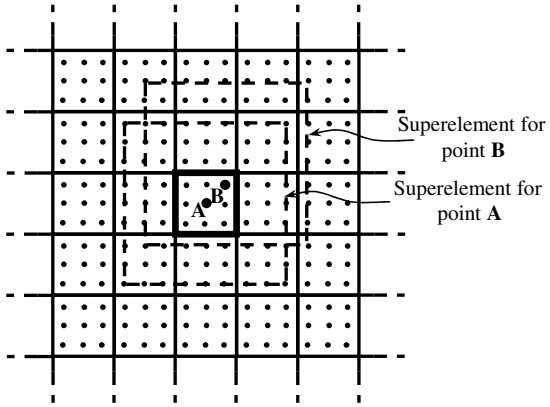

Fig. 4 Schematic illustration for the computation of the Laplacian terms from a regular finite element mesh.

because the resulting partial deferential equations hold in the whole body.

In classical inelasticity, the inelastic multipliers are calculated by restoring the consistency condition iteratively. However, it is not possible for the nonlocal formulation, because it depends on high-order gradients. To evaluate the gradients $\nabla^2\dot{\lambda}^{vp}$ and $\nabla^2\dot{\lambda}^{vd}$ at integration point m, the values of $\dot{\lambda}^{vp}$ and $\dot{\lambda}^{vd}$ at m, as well as the values at the neighboring points (nonlocality), are needed. The gradient at m is evaluated from the derivatives of a polynomial function that interpolates the values of the inelastic multiplier at the neighboring points. Therefore, the gradient terms $\nabla^2\dot{\lambda}^{vp}$ and $\nabla^2\dot{\lambda}^{vd}$ can be expressed in terms of $\dot{\lambda}_n^{vp}$ and $\dot{\lambda}_n^{vd}$ with $n \in \{1, \ldots, N_{GP}\}$ using the following relations:

$$\nabla^2\dot{\lambda}_m^{vp} = \sum_{n=1}^{N_{\mathrm{GP}}} \bar{g}_{mn}\dot{\lambda}_n^{vp}; \qquad \nabla^2\dot{\lambda}_m^{vd} = \sum_{n=1}^{N_{\mathrm{GP}}} \bar{g}_{mn}\dot{\lambda}_n^{vd} \tag{44}$$

where N_{GP} is the number of Gauss integration points. The computation of coefficients $\bar{g}_{mn}$ is explained in what follows.

Figure 4 shows a schematic illustration for the computation of the Laplacian terms from a regular finite element mesh, where $\nabla^2\dot{\lambda}^{vp}$ and $\nabla^2\dot{\lambda}^{vd}$ are needed at the integration points of each element. For two-dimensional problems, a four-node element with nine integration points (full integration) is assumed. Eight elements (superelement) are used to compute $\nabla^2\dot{\lambda}^{vp}$ and $\nabla^2\dot{\lambda}^{vd}$ at each integration point; which means that 81 integration points are used to calculate the gradients at each integration point. Except for each corner and midboundary elements, their nine integration points are used to calculate the gradients. This illustration is valid for any element with any number of integration points. However, with more integration points, higher accuracy is achieved. This illustration is valid for one-dimensional, as well as for three-dimensional, mesh discretizations.

To determine the coefficients $\bar{g}_{mn}$, a complete second-order polynomial function is used to evaluate the inelastic multipliers around point m, such that

$$\dot{\lambda} = \boldsymbol{a}^T\boldsymbol{v} \tag{45}$$

where $\dot{\lambda}$ could be $\dot{\lambda}^{vp}$ or $\dot{\lambda}^{vd}$, $\boldsymbol{a}$ is the coefficients vector, and $\boldsymbol{v}$ is the variables vector. For example, in two-dimensional problems, one has the following expressions for $\boldsymbol{a}$ and $\boldsymbol{v}$: $\boldsymbol{a}^T = \lfloor a_1\ a_2\ a_3\ a_4\ a_5\ a_6 \rfloor$ and $\boldsymbol{v}^T = \lfloor 1\ x\ y\ xy\ x^2\ y^2 \rfloor$.

To obtain the coefficients vector $\boldsymbol{a}$, a minimization method by least squares is used. Moreover, the interpolation is made in the global coordinate system (x, y, z) of the generated mesh with N_{GP} integration points. The coefficients vector $\boldsymbol{a}$ can be expressed in the following form:

$$\boldsymbol{\Lambda} = \boldsymbol{M}^T\boldsymbol{a} \tag{46}$$

For a two-dimensional mesh, the matrix $\boldsymbol{M}$ and the inelastic multipliers vector $\boldsymbol{\Lambda}$ are defined by

$$\boldsymbol{M} = \begin{bmatrix} 1 & 1 & \cdots & 1 \\ x_1 & x_2 & \cdots & x_{N_{\mathrm{GP}}} \\ y_1 & y_2 & \cdots & y_{N_{\mathrm{GP}}} \\ x_1y_1 & x_2y_2 & \cdots & x_{N_{\mathrm{GP}}}y_{N_{\mathrm{GP}}} \\ x_1^2 & x_2^2 & \cdots & x_{N_{\mathrm{GP}}}^2 \\ y_1^2 & y_2^2 & \cdots & y_{N_{\mathrm{GP}}}^2 \end{bmatrix} \tag{47}$$

and $\boldsymbol{\Lambda} = \lfloor \dot{\lambda}_1\ \dot{\lambda}_2\ \cdots\ \dot{\lambda}_{N_{\mathrm{GP}}} \rfloor^T$.

Multiplying both sides of Eq. (46) by $\boldsymbol{M}$, one can write

$$\boldsymbol{M}\boldsymbol{\Lambda} = \boldsymbol{H}\boldsymbol{a} \tag{48}$$

where $\boldsymbol{H} = \boldsymbol{M}\boldsymbol{M}^T$ is a symmetrical square matrix and can be written for two-dimensional problems as

$$\boldsymbol{H} = \sum_{n=1}^{N_{\mathrm{GP}}} \begin{bmatrix} 1 & x_n & y_n & x_ny_n & x_n^2 & y_n^2 \\ & x_n^2 & x_ny_n & x_n^2y_n & x_n^3 & x_ny_n^2 \\ & & y_n^2 & x_ny_n^2 & x_n^2y_n & y_n^3 \\ & & & x_n^2y_n^2 & x_n^3y_n & x_ny_n^3 \\ & \text{symm} & & & x_n^4 & x_n^2y_n^2 \\ & & & & & y_n^4 \end{bmatrix} \tag{49}$$

It is obvious that $\boldsymbol{H}$ needs to be updated at each loading increment for finite deformation problems.

From Eqs. (45) and (48), one can then compute the inelastic multiplier vector and its Laplacian, respectively, as follows:

$$\dot{\lambda} = \boldsymbol{a}^T\boldsymbol{v} = (\boldsymbol{H}^{-1}\boldsymbol{M}\boldsymbol{\Lambda})^T\boldsymbol{v} = \left(\boldsymbol{H}^{-1}\sum_{n=1}^{N_{\mathrm{GP}}}\dot{\lambda}_n\boldsymbol{v}_n\right)^T\boldsymbol{v} \tag{50}$$

$$\nabla^2\dot{\lambda} = \left(\boldsymbol{H}^{-1}\sum_{n=1}^{N_{\mathrm{GP}}}\dot{\lambda}_n\boldsymbol{v}_n\right)^T\nabla\boldsymbol{v} \tag{51}$$

For the integration point m, one can write expressions for

$$\nabla^2\dot{\lambda}_m = \nabla_{xx}\dot{\lambda}_m + \nabla_{yy}\dot{\lambda}_m + \nabla_{zz}\dot{\lambda}_m \tag{52}$$

as follows

$$\nabla^2\dot{\lambda}_m = \sum_{n=1}^{N_{\mathrm{GP}}}(\boldsymbol{v}_n^T\boldsymbol{H}^{-1}\nabla_{xx}\boldsymbol{v}_m + \boldsymbol{v}_n^T\boldsymbol{H}^{-1}\nabla_{yy}\boldsymbol{v}_m + \boldsymbol{v}_n^T\boldsymbol{H}^{-1}\nabla_{zz}\boldsymbol{v}_m)\dot{\lambda}_n \tag{53}$$

Comparing Eqs. (44) with Eq. (53), $\bar{g}_{mn}$ can be computed using the following expression:

$$\bar{g}_{\,mn} = \boldsymbol{v}_n^T\boldsymbol{H}^{-1}\nabla_{xx}\boldsymbol{v}_m + \boldsymbol{v}_n^T\boldsymbol{H}^{-1}\nabla_{yy}\boldsymbol{v}_m + \boldsymbol{v}_n^T\boldsymbol{H}^{-1}\nabla_{zz}\boldsymbol{v}_m \tag{54}$$

The coefficients $\bar{g}_{mn}$ depend only on the x, y, and z updated coordinates of the Gauss integration points. These coefficients are computed at each loading increment for finite deformations.

Using Eqs. (44) and (54), one can now nonlocally determine $\dot{\lambda}^{vp}$ and $\dot{\lambda}^{vd}$ at each integration point m from the generalized consistency conditions (31) and (38). This is shown in the subsequent development.

Nonlocal Computational Algorithm

By substituting Eqs. (44) into Eqs. (31) and (38), one can rewrite the generalized viscoplasticity consistency condition (31) and the generalized viscodamage consistency condition (38) at each integration point m, respectively, as follows:

$$\left(\frac{\partial f}{\partial\boldsymbol{\tau}_{(m)}^{(i)}}:\boldsymbol{C}_{(m)}^{(i)} + \boldsymbol{Z}_{(m)}^{p(i)}\right):\boldsymbol{d}_{(m)} + Q_{1(m)}^{p(i)}\dot{\lambda}_{(m)}^{vp} + Q_{2(m)}^{p(i)} \times \sum_{n=1}^{N_{\mathrm{GP}}}\bar{g}_{(mn)}\dot{\lambda}_{(n)}^{vp} + Q_{3(m)}^{p(i)}\dot{\lambda}_{(m)}^{vd} + Q_{4(m)}^{p(i)}\sum_{n=1}^{N_{\mathrm{GP}}}\bar{g}_{(mn)}\dot{\lambda}_{(n)}^{vd} = 0 \tag{55}$$

$$\left(\frac{\partial g}{\partial\boldsymbol{\tau}_{(m)}^{(i)}}:\boldsymbol{C}_{(m)}^{(i)} + \boldsymbol{Z}_{(m)}^{d(i)}\right):\boldsymbol{d}_{(m)} + Q_{1(m)}^{d(i)}\dot{\lambda}_{(m)}^{vp} + Q_{2(m)}^{d(i)} \times \sum_{n=1}^{N_{\mathrm{GP}}}\bar{g}_{(mn)}\dot{\lambda}_{(n)}^{vp} + Q_{3(m)}^{d(i)}\dot{\lambda}^{vd} + Q_{4(m)}^{d(i)}\sum_{n=1}^{N_{\mathrm{GP}}}\bar{g}_{(mn)}\dot{\lambda}_{(n)}^{vd} = 0 \tag{56}$$

Note that m indicates the integration point and i indicates the previous iteration number.

Let us define the following expressions

$$\mathbb{R}_{(m)}^{p(i)} = \left(\frac{\partial f}{\partial\boldsymbol{\tau}_{(m)}^{(i)}}:\boldsymbol{C}_{(m)}^{(i)} + \boldsymbol{Z}_{(m)}^{p(i)}\right):\boldsymbol{d}_{(m)} \tag{57}$$

$$\mathbb{R}^{d(i)}_{(m)} = \left(\frac{\partial g}{\partial \boldsymbol{\tau}^{(i)}_{(m)}} : \boldsymbol{C}^{(i)}_{(m)} + \boldsymbol{Z}^{d(i)}_{(m)} \right) : \boldsymbol{d}_{(m)} \tag{58}$$

$$\boldsymbol{G}^{pp(i)} = \begin{bmatrix} Q^{p(i)}_{1(1)} + Q^{p(i)}_{2(1)}\bar{g}_{11} & Q^{p(i)}_{2(2)}\bar{g}_{12} & \cdots & Q^{p(i)}_{2(N_{\mathrm{GP}})}\bar{g}_{1N_{\mathrm{GP}}} \\ Q^{p(i)}_{2(2)}\bar{g}_{21} & Q^{p(i)}_{1(2)} + Q^{p(i)}_{2(2)}\bar{g}_{22} & \cdots & Q^{p(i)}_{2(N_{\mathrm{GP}})}\bar{g}_{2N_{\mathrm{GP}}} \\ \vdots & \vdots & \ddots & \vdots \\ Q^{p(i)}_{2(N_{\mathrm{GP}})}\bar{g}_{N_{\mathrm{GP}}1} & Q^{p(i)}_{2(N_{\mathrm{GP}})}\bar{g}_{2N_{\mathrm{GP}}} & \cdots & Q^{p(i)}_{1(N_{\mathrm{GP}})} + Q^{p(i)}_{2(N_{\mathrm{GP}})}\bar{g}_{N_{\mathrm{GP}}N_{\mathrm{GP}}} \end{bmatrix} \tag{59}$$

$$\boldsymbol{G}^{pd(i)} = \begin{bmatrix} Q^{p(i)}_{3(1)} + Q^{p(i)}_{4(1)}\bar{g}_{11} & Q^{p(i)}_{4(2)}\bar{g}_{12} & \cdots & Q^{p(i)}_{4(N_{\mathrm{GP}})}\bar{g}_{1N_{\mathrm{GP}}} \\ Q^{p(i)}_{4(2)}\bar{g}_{21} & Q^{p(i)}_{3(2)} + Q^{p(i)}_{4(2)}\bar{g}_{22} & \cdots & Q^{p(i)}_{4(N_{GP})}\bar{g}_{2N_{\mathrm{GP}}} \\ \vdots & \vdots & \ddots & \vdots \\ Q^{p(i)}_{4(N_{\mathrm{GP}})}\bar{g}_{N_{\mathrm{GP}}1} & Q^{p(i)}_{4(N_{\mathrm{GP}})}\bar{g}_{2N_{\mathrm{GP}}} & \cdots & Q^{p(i)}_{3(N_{\mathrm{GP}})} + Q^{p(i)}_{4(N_{\mathrm{GP}})}\bar{g}_{N_{\mathrm{GP}}N_{\mathrm{GP}}} \end{bmatrix} \tag{60}$$

$$\boldsymbol{G}^{dp(i)} = \begin{bmatrix} Q^{d(i)}_{1(1)} + Q^{d(i)}_{2(1)}\bar{g}_{11} & Q^{d(i)}_{2(2)}\bar{g}_{12} & \cdots & Q^{d(i)}_{2(N_{\mathrm{GP}})}\bar{g}_{1N_{\mathrm{GP}}} \\ Q^{d(i)}_{2(2)}\bar{g}_{21} & Q^{d(i)}_{1(2)} + Q^{d(i)}_{2(2)}\bar{g}_{22} & \cdots & Q^{d(i)}_{2(N_{\mathrm{GP}})}\bar{g}_{2N_{\mathrm{GP}}} \\ \vdots & \vdots & \ddots & \vdots \\ Q^{d(i)}_{2(N_{\mathrm{GP}})}\bar{g}_{N_{\mathrm{GP}}1} & Q^{d(i)}_{2(N_{\mathrm{GP}})}\bar{g}_{2N_{\mathrm{GP}}} & \cdots & Q^{d(i)}_{1(N_{\mathrm{GP}})} + Q^{d(i)}_{2(N_{\mathrm{GP}})}\bar{g}_{N_{\mathrm{GP}}N_{\mathrm{GP}}} \end{bmatrix} \tag{61}$$

$$\boldsymbol{G}^{dd(i)} = \begin{bmatrix} Q^{d(i)}_{3(1)} + Q^{d(i)}_{4(1)}\bar{g}_{11} & Q^{d(i)}_{4(2)}\bar{g}_{12} & \cdots & Q^{d(i)}_{4(N_{\mathrm{GP}})}\bar{g}_{1N_{\mathrm{GP}}} \\ Q^{d(i)}_{4(2)}\bar{g}_{21} & Q^{d(i)}_{3(2)} + Q^{d(i)}_{4(2)}\bar{g}_{22} & \cdots & Q^{d(i)}_{4(N_{\mathrm{GP}})}\bar{g}_{2N_{\mathrm{GP}}} \\ \vdots & \vdots & \ddots & \vdots \\ Q^{d(i)}_{4(N_{\mathrm{GP}})}\bar{g}_{N_{\mathrm{GP}}1} & Q^{d(i)}_{4(N_{\mathrm{GP}})}\bar{g}_{2N_{\mathrm{GP}}} & \cdots & Q^{d(i)}_{3(N_{\mathrm{GP}})} + Q^{d(i)}_{4(N_{\mathrm{GP}})}\bar{g}_{N_{\mathrm{GP}}N_{\mathrm{GP}}} \end{bmatrix} \tag{62}$$

$$\boldsymbol{\Lambda}^{vp} = \lfloor\, \dot{\lambda}^{vp}_1 \quad \dot{\lambda}^{vp}_2 \quad \cdots \quad \dot{\lambda}^{vp}_{N_{\mathrm{GP}}} \,\rfloor^T \tag{63}$$

$$\boldsymbol{\Lambda}^{vd} = \lfloor\, \dot{\lambda}^{vd}_1 \quad \dot{\lambda}^{vd}_2 \quad \cdots \quad \dot{\lambda}^{vd}_{N_{\mathrm{GP}}} \,\rfloor^T \tag{64}$$

$$\mathbb{R}^{p(i)} = \lfloor\, \mathbb{R}^{p(i)}_1 \quad \mathbb{R}^{p(i)}_2 \quad \cdots \quad \mathbb{R}^{p(i)}_{N_{\mathrm{GP}}} \,\rfloor^T \tag{65}$$

$$\mathbb{R}^{d(i)} = \lfloor\, \mathbb{R}^{d(i)}_1 \quad \mathbb{R}^{d(i)}_2 \quad \cdots \quad \mathbb{R}^{d(i)}_{N_{\mathrm{GP}}} \,\rfloor^T \tag{66}$$

One can then write Eqs. (55) and (56), respectively, as follows:

$$\boldsymbol{G}^{pp(i)}\boldsymbol{\Lambda}^{vp} + \boldsymbol{G}^{pd(i)}\boldsymbol{\Lambda}^{vd} = \mathbb{R}^{p(i)} \tag{67}$$

$$\boldsymbol{G}^{dp(i)}\boldsymbol{\Lambda}^{vp} + \boldsymbol{G}^{dd(i)}\boldsymbol{\Lambda}^{vd} = \mathbb{R}^{d(i)} \tag{68}$$

Combining Eqs. (67) and (68), one obtains

$$\begin{bmatrix} \boldsymbol{G}^{pp(i)} & \boldsymbol{G}^{pd(i)} \\ \boldsymbol{G}^{dp(i)} & \boldsymbol{G}^{dd(i)} \end{bmatrix} \begin{Bmatrix} \boldsymbol{\Lambda}^{vp} \\ \boldsymbol{\Lambda}^{vd} \end{Bmatrix} = \begin{Bmatrix} \mathbb{R}^{p(i)} \\ \mathbb{R}^{d(i)} \end{Bmatrix} \tag{69}$$

The preceding linear system of equations can be solved for $\boldsymbol{\Lambda}^{vp}$ and $\boldsymbol{\Lambda}^{vd}$ using a numerical iterative scheme such as the Gauss–Jordan iterative method. The viscoplastic and viscodamage multipliers are obtained when the viscoplasticity and viscodamage conditions f and g are fulfilled at the end of the loading step for a suitable tolerance, such that

$$\sum_{n=1}^{N_{\mathrm{GP}}} f_n \le \mathrm{tol} \quad \text{and} \quad \sum_{n=1}^{N_{\mathrm{GP}}} g_n \le \mathrm{tol} \tag{70}$$

where tol could be set to a very small value, on the order of 10^{-5}.

Note that in the undamaged elastic elements $\dot{\lambda}^{vp}_m = 0$ and $\dot{\lambda}^{vd}_m = 0$; however, for spreading of the inelastic zone, it is important that the numerical solution allows $\nabla^2\dot{\lambda}^{vp}_m > 0$ and $\nabla^2\dot{\lambda}^{vd}_m > 0$ at the elastic–inelastic boundary. If inelastic integration points appear in the structure, then in the elastic integration points adjacent to the inelastic zone, one has nonzero $\boldsymbol{\Lambda}$ (Fig. 3). Therefore, the proposed algorithm has a feature that these elastic integration points have $\dot{\lambda}^{vp}_m \approx 0$ and $\nabla^2\dot{\lambda}^{vp}_m > 0$ and/or $\dot{\lambda}^{vd}_m \approx 0$ and $\nabla^2\dot{\lambda}^{vd}_m > 0$. As a result, the yield strength is increased/decreased and the damage at these elastic points is delayed (hardening) or enters the softening region.

The preceding algorithm for gradient-dependent inelasticity appears to have several advantages over the standard algorithm by de Borst and his coworkers [47,48] with regard to the incorporation of the gradient-dependent model in a finite element code. The proposed computational algorithm can be implemented in the existing finite element codes without large modifications, compared with the computational approach of de Borst and his coworkers. In contrast to

Table 1 Material constants for target and projectile materials

Target material of Weldox 460E steel			
$E = 200$ GPa	$a_1 = 400$ MPa	$h_1 = 0$	$r_0 = 0$
$\nu = 0.33$	$a_2 = 20$ GPa	$h_2 = 0$	$\gamma = 1.7$
$\bar{Y}_o = 490$ MPa	$a_3 = 0$	$\Upsilon = 0.9$	$m = 0.94$
$T_r = 295$ K	$a_4 = 0$	$\ell = 5\ \mu$m	$n = 1$
$T_m = 1800$ K	$k_1 = 0.1$ MPa^{-1}	$\alpha_t = 1.1 \times 10^{-5}$/K	$\phi_{\text{eq}}^c = 0.30$
$\rho_o = 7850$ kg/m^3	$k_2 = 15$ GPa^{-1}	$c_p = 452$ J/kg · K	$P_{\text{cutoff}} = 160$ GPa
$\eta^v = 0.01$ s	$\eta_r = 0$	$c_v = 266$ J/kg · K	
Projectile material of hardened Arne tool steel			
$E = 204$ GPa	$\nu = 0.33$	$\rho_o = 7850$ kg/m^3	$Y_o = 1900$ MPa
$E_t = 15$ GPa	$\varepsilon_f = 2.15\%$		

the latter approach, for calculation of the gradient terms, one does not need to introduce shape functions of the C^1 class or penalty-enhanced C^o class functions for the interpolation of the Laplacian terms. This is because the governing constitutive equations in the proposed approach are replaced directly by the difference equations of the field variables and no interpolation functions are needed for the gradient terms.

Numerical Applications

The current constitutive microdamage model and the proposed numerical integration algorithm is implemented in the explicit commercial finite element code ABAQUS/Explicit [39] using the user material subroutine VUMAT. The ABAQUS/Explicit is mainly used for high transient dynamic problems and it uses explicit integration algorithms.

The computational model presented in the previous sections is used here to model a blunt projectile impacting a target. The objective of this numerical example is to investigate if the proposed constitutive equations are able to describe the structural response to projectile impact damage when different failure modes are expected to occur. This is done by conducting numerical simulation of the experimental tests presented by Borvik et al. [23] for a blunt projectile made of hardened Arne tool steel impacting a circular plate made of Weldox 460E steel. For more detailed information regarding the numerical scheme, such as the contact-impact algorithm, the automatic mesh generator, the ALE adaptive meshing, and the element erosion algorithm, the reader is referred to the manuals of ABAQUS/Explicit [39].

For simplicity, the projectile is modeled as a bilinear elastic–plastic strain-rate-independent von Mises material with isotropic hardening, which is already implemented in ABAQUS/Explicit code. The model material constants of the target material of Weldox 460E steel and the projectile material of hardened Arne tool steel are listed in Table 1. These material constants are determined based on the following considerations.

Although there has been a considerable work to understand the physical role of the gradient theory, this research area is still in a critical state with controversy. This is to some extent due to the difficulty in identifying the magnitude of the material length scale ℓ associated with the gradient-dependent models. More important is the difficulty of carrying out truly definitive experiments on critical aspects of the evolution of the dislocation, crack, and void structures. Furthermore, the determination of ℓ should be based on information from micromechanical gradient-dominant tests such as micro/nanoindentation tests, microbending tests, and microtorsion tests. Abu Al-Rub and Voyiadjis [40,41] presented a physically based approach for identification of the material length scales ℓ from microindentation, microbending, and/or microtorsion tests. Therefore, the values for ℓ listed in Table 1 are identified using this approach. The values for E, ν, T_r, T_m, α_t, ρ_o, c_v, c_p, Υ, η^v, m, n, and ϕ_{eq}^c are as reported by Borvik et al. [23]. The material constants a_1 and k_1 associated with the plasticity isotropic hardening are identified from tensile tests [49], whereas the material constants a_2 and k_2 associated with the plasticity kinematic hardening are identified from a strain-control cyclic-hardening test [50]. Damage initiation is assumed to occur at the beginning of loading, such that $r_0 = 0$. The damage isotropic and kinematic hardening is assumed negligible, such that $a_3 = a_4 = 0$ and $h_1 = h_2 = 0$, respectively. The material constants b_1 and b_2 are identified as $b_1 = \frac{1}{2} a_1 \ell^2$ and $b_2 = \frac{1}{2} a_2 \ell^2$. The material constants used for the hardened Arne tool steel are the same as those reported in [23,24]. The material constants listed in Table 1 are used to conduct the following simulations.

In these simulations, a four-node 2-D axisymmetric element with one integration point and a stiffness based on hourglass control is used. A plot of the initial configuration, showing a part of the target plate and the blunt projectile just before impact, is shown in Fig. 5. The target plate has a nominal thickness of 12 mm and a diameter of 500 mm, whereas the nominal length and diameter of the hardened projectile are 80 and 20 mm, respectively. In each run, the target plate is fully clamped at the support, whereas the projectile is given an initial velocity similar to the one used in the corresponding experiment conducted by Borvik et al. [23]. The initial size of the smallest element in the impact region is 0.25×0.2 mm^2 in all simulations, giving a total of 60 elements over the target thickness. To reduce the computational time, which is affected both by the element size and number, the mesh was somewhat coarsened toward the boundary. Owing to this coarsening, the total number of elements in the target plate is less than about 10,000 in the simulations. Contact was modeled using an automatic 2-D single-surface penalty formulation available in ABAQUS/Explicit [39]. A friction coefficient of 0.05 is assumed between the projectile and the target. Time increments of the order of 10^{-8} s are used to satisfy the stability criteria.

Adaptive meshing techniques have received tremendous attention during the last decade to solve high-speed-impact damage problems. The coupled ALE is used to extend the domain of application in the Lagrangian codes. The advantages of using adaptive meshing in high-speed-impact damage-penetration problems are many. It enables the simulation of large inelastic flow in the Lagrangian framework. It may also include the possibility to obtain a solution of comparable accuracy using much fewer elements, and hence less computational resources than with a fixed mesh. Also, it prevents severe mesh distortions and unacceptable small time steps in the simulations. However, the major disadvantage of this method is the possible introduction of inaccuracies and smoothening of the results

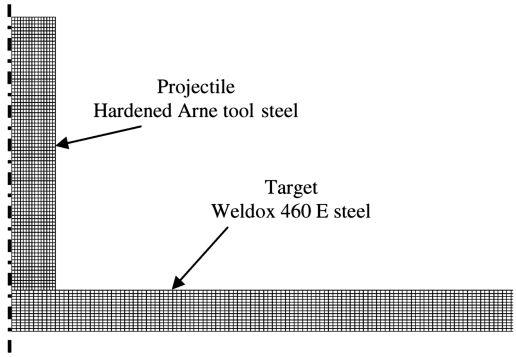

Fig. 5 Finite element mesh plot of the axisymmetric initial configuration just before impact.

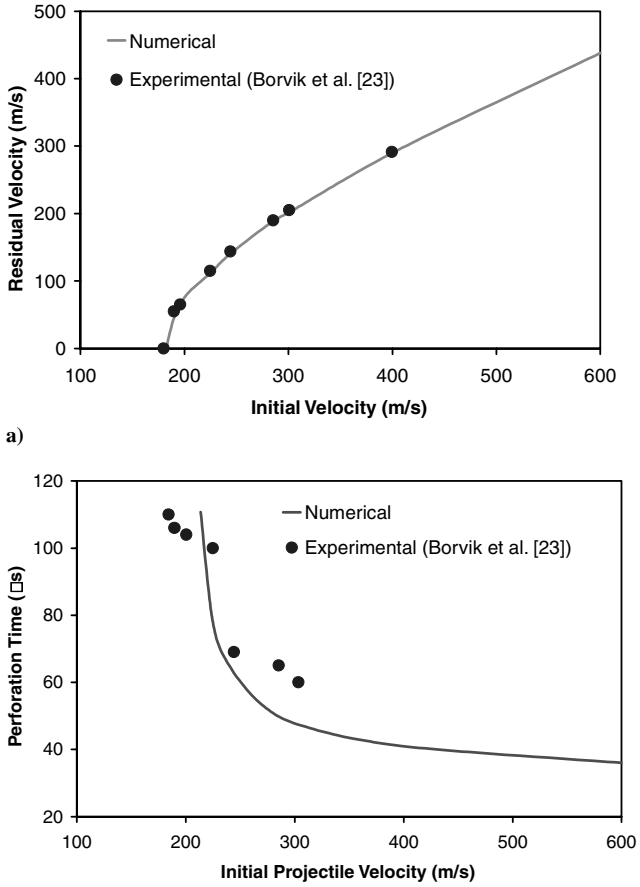

Fig. 6 Comparison between numerical and experimental results by a blunt projectile for a) the initial impact velocity vs residual projectile velocity and b) perforation times vs initial impact velocities.

during mapping of the history variables. Adaptive meshing is used in the following simulations, in which 10 adaptive refinements are used in each run.

Borvik et al. [49] simulations indicated the problem involving shear localization and plugging for blunt projectiles to be mesh-size-sensitive. However, the numerical solution using the present model is mesh-size-independent and converges monotonically toward a limit solution when the number of elements over the target thickness becomes sufficiently large. Therefore, the numerical results improve as the element size is reduced, until it stabilizes at some value (i.e., the mesh size dependency is not pathological). This is expected because the width of the shear band is known to be on the order of 10–100 μm [51].

A direct comparison between the numerical and experimental residual velocity curves for blunt projectiles is shown in Fig. 6a. As

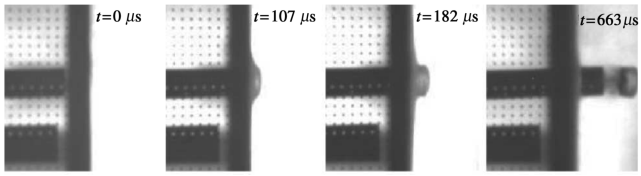

Fig. 7 High-speed-camera images showing perforation of the target plate at impact velocities close to the ballistic limits with a blunt projectile (after Borvik et al. [23]).

seen, there is a good agreement with the experimental results. Moreover, Fig. 6b shows that the perforation times obtained from the different numerical simulations are similar and close to the experimental values estimated from high-speed-camera images obtained by Borvik et al. [23]. It is noteworthy that Fig. 6a cannot be a direct derivative of Fig. 6b, because the projectile is deformable and the plasticity and damage interaction mechanisms (nonlinearity) in the plate are considered. All these factors are affecting the perforation time so that one cannot simply obtain the perforation time by knowing the initial and residual velocities of the projectile and the target thickness. For example, for 303.5 m/s impact velocity, the residual velocity from Fig. 6a is 199.7 m/s. By linear kinematics and knowing that the target thickness is 12 mm, one can simply calculate the perforation time to be 116 μs, whereas experimentally it is reported as 60 μs, which deviates from the calculated one.

High-speed-camera images of perforation of the target plate at impact velocities close to the ballistic limit are shown in Fig. 7. Numerical plots of perforation of the target plate by a blunt projectile at impact velocity close to the ballistic limit of 210 m/s are shown in Fig. 8. The contours of accumulated viscoinelastic strain are plotted on the deformed mesh. It can be seen that limited inelastic deformation occurs outside the localized shear zone. These plots clearly demonstrate that the numerical model qualitatively captures the overall physical behavior of the target during penetration and perforation. Notice also that in these plots, only a part of the complete target plate is shown.

The elements in the impacted area are significantly distorted. However, stable results are nevertheless obtained. This delayed the damage evolution process and, consequently, the erosion of damaged elements. However, the upper nodes in a critical element do not penetrate the lower nodes, giving a stable solution, and no error termination is encountered in the code. Figure 9 shows the element distortion in the target plate just after impact. Figure 10 shows the target rear surface, for which complete perforation did not occur.

The final cross section of a target plate perforated by a blunt projectile at an impact velocity close to the ballistic limit is shown in Fig. 11, which is very similar to the experimental cross section obtained by Borvik et al. [23].

In general, it can be seen that close agreement between the numerical and experimental results is achieved. Hence, the computational methodology presented in this paper works well for ductile targets perforated by deformable blunt projectiles. However, different sets of experiments need to be simulated to draw solid

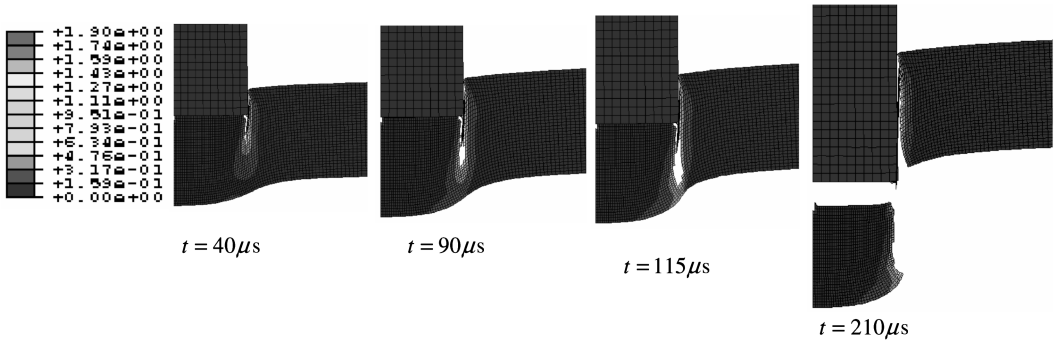

Fig. 8 Perforation of the target plate by a blunt projectile of initial impact velocity of 210 m/s plotted as contours of accumulated inelastic strain and at different times. The light-colored region indicates an accumulated damage between 0.25 and 0.30.

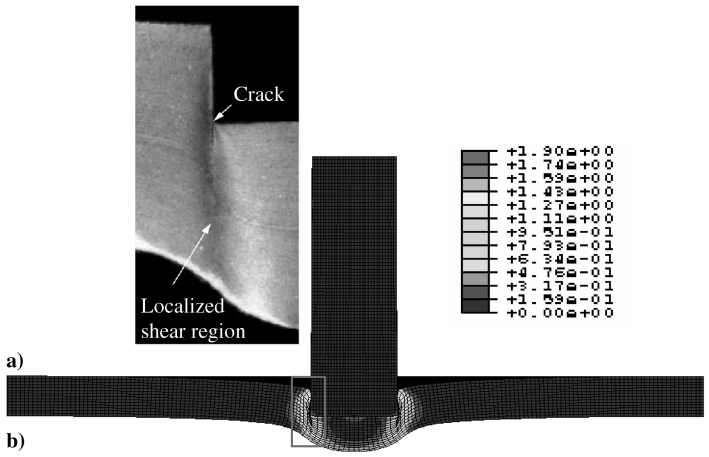

Fig. 9 Penetration of the target plate by a blunt projectile of initial impact velocity of 300 m/s: a) macrograph of sectioned and etched target plate close to perforation (after Borvik et al. [23]) and b) simulation plotted as contours of accumulated inelastic strain.

Fig. 10 Target rear surface for which complete perforation did not occur: a) experimental (after Borvik et al. [23]) and b) numerical.

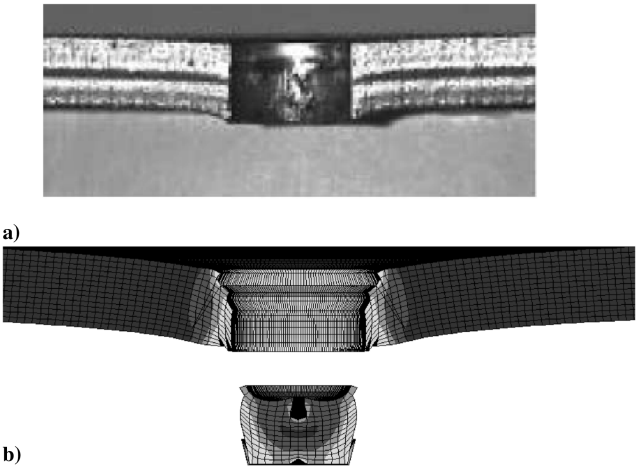

Fig. 11 Final cross section of the target plate perforated by a blunt projectile of initial impact velocity of 300 m/s: a) experimental (after Borvik et al. [23]) and b) numerical.

conclusions. More elaborate study using the current gradient-dependent viscoplastic and viscodamage model is needed for simulating high-speed impacts of different target thicknesses and also using different projectile nose shapes (e.g., hemispherical and conical). This is not the subject of this paper but will be presented in detail in a forthcoming paper by the authors. However, the proposed theoretical and computational work can be used to study long or short penetrators, thin or thick targets, normal or oblique impacts, ductile or brittle materials, different velocity regions, different types of projectiles, etc.

The aforementioned advantages provided by the nonlocal theory do lead to an improvement in the modeling and numerical simulation of high-velocity-impact-related problems. The study of strain localization and its regularization on impact-damage-related problems needs further attention to allow one to properly simulate impact damage problems without conducting extensive experiments.

Conclusions

In this study, it was recognized that the initiation and propagation of the microdefects depend on both the amplitude and distribution of the inelastic strains/stress in the vicinity around the microdefects. This implies that the evolution of the material inelasticity is practically a nonlocal process. These observations indicate that there is a need for such a micromechanical approach that incorporates material-length-scale parameters into the classical constitutive relations. The incorporation of spatial higher-order gradient terms allows one to introduce a "missing" length scale into the classical continuum theories, allowing the size effect to be captured.

A gradient-enhanced (nonlocal) coupled rate-dependent plasticity and damage model is developed in this work on the continuum level to bridge the gap between the micromechanical and classical continuum inelasticity. The thermodynamic consistency of the gradient-dependent plasticity/damage constitutive relations is discussed thoroughly in [27,28,30]. Implicit and explicit incorporation of material length scales is achieved through the development of coupled viscoinelasticity (rate-dependent plasticity/damage) and gradient-dependent (nonlocal) constitutive relations, respectively. Therefore, the resulting model incorporates, in a very modular fashion, the damage and plasticity effects in solids and, most important, in a physically based and motivated approach.

Several numerical algorithms are developed in this work to integrate the highly nonlinear differential equations effectively and to optimize the computational performance. In this work, a return-mapping algorithm is used for the integration of the proposed model, remarkably, sharing the exact same structure as the classical return mapping employed in the integration of rate-independent plasticity/damage and gradient-independent plasticity/damage. An operator split structure consisting of a trial state followed by the return map is developed by imposing generalized (rate-independent to rate-dependent) viscoplastic and viscodamage consistency conditions simultaneously; this allows one to integrate both rate-dependent and rate-independent models in a similar fashion. Moreover, a simple and direct computational algorithm is also used for the calculation of the Laplacian gradients, allowing one to integrate both the gradient-dependent and gradient-independent models in a similar way. Furthermore, a trivially incrementally objective integration scheme is proposed. The proposed finite deformation scheme is based on hypoelastic stress–strain representations and the proposed hypoelastic predictor and coupled viscoplastic–viscodamage corrector algorithm that allows for total uncoupling of the geometrical and material nonlinearities. The nonlinear algebraic

system of equations is solved by consistent linearization and the use of the Newton–Raphson iteration. The numerical implementation then involves a series of coupled routines that provide the stresses and updates of the corresponding internal variables.

The constitutive model and numerical integration algorithms are implemented in the well-known explicit finite element code ABAQUS/Explicit using the material subroutine VUMAT. In this paper, the application of the proposed model to the numerical simulation of localization and formation of shear bands in structures subjected to high-speed-impact loading conditions is presented. Good agreement is obtained between the numerical simulations and experimental results. The material length scale proposed in this work has the potential to predict the size effects in material failure.

It is noted that the material length parameter ℓ controls the initial yield strength, the hardening of the material, the softening behavior, and it slows down the damage evolution. More detailed parametric study for the effect of the material length scale will be presented in a forthcoming paper by the authors.

Acknowledgment

Financial support for this research has been provided by the U.S. Air Force Office of Scientific Research through the U.S. Air Force Institute of Technology at Wright–Patterson Air Force Base under grant number F33601-01-P-0343.

References

[1] Anderson, C. E., "Proceedings of the 2003 Hypervelocity Impact Symposium," *International Journal of Impact Engineering*, Vol. 29, No. 1–10, 2003, pp. 1–867.

[2] Yatteau, J. D., Recht, G. W., and Edquits, K. T., "Transverse Loading and Response of Long Rod Penetrators During High Velocity Plate Perforation," *International Journal of Impact Engineering*, Vol. 23, 1999, pp. 967–980.

[3] Hayhurst, C. J., Livingstone, I. H. G., Clegg, R. A., Destefanis, R., and Faraud, M., "Ballistic Limit Evaluation of Advanced Shielding Using Numerical Simulations," *International Journal of Impact Engineering*, Vol. 26, 2001, pp. 309–320.

[4] Knudson, M. D., Hall, C. A., Lemke, R., Deeney, C., and Asay, J. R., "High Velocity Flyer Plate Launch Capability on the Sandia Z Accelerator," *International Journal of Impact Engineering*, Vol. 29, 2003, pp. 377–384.

[5] Zukas, J. A., *High Velocity Impact Dynamics*, Wiley, New York, 1990.

[6] Christiansen, E. L., and Friesen, L., "Penetration Equations for Thermal Protection Materials," *International Journal of Impact Engineering*, Vol. 20, 1997, pp. 153–164.

[7] Christiansen, E. L., and Kerr, J. H., "Projectile Shape Effects on Shielding Performance at 7 km/s and 11 km/s," *International Journal of Impact Engineering*, Vol. 20, 1997, pp. 165–172.

[8] Benson, D. J., "Computational Methods in Lagrangian and Eulerian Hydrocodes," *Computer Methods in Applied Mechanics and Engineering*, Vol. 99, 1992, pp. 235–394.

[9] McGlaun, J. M., Thompson, S. L., and Elrick, M. G., "CTH: A Three Dimensional Shock Wave Physics Code," *International Journal of Impact Engineering*, Vol. 10, 1990, pp. 351–360.

[10] Hallquist, J. O., *Theoretical Manual for DYNA3-D*, Lawrence Livermore National Lab., Livermore, CA, 1983.

[11] Carroll, D. E., Hertel, E. S., and Trucano, T. G., "Simulation of Armor Penetration by Tungsten Rods: ALEGRA Validation Report," Sandia National Labs., Rept. SAND97-2765, Albuquerque, NM, 1997.

[12] Stellingwerf, R. F., and Wingate, C. A., "Impact Modeling with Smooth Particle Hydrodynamics," *International Journal of Impact Engineering*, Vol. 14, 1993, pp. 707–718.

[13] Belytschko, T., Krongauz, Y., Organ, D., Fleming, M., and Krysl, P., "Meshless Methods: an Overview and Recent Developments," *Computer Methods in Applied Mechanics and Engineering*, Vol. 139, 1996, pp. 3–47.

[14] Fahrenthold, E. P., and Horban, B. A., "An Improved Hybrid Particle–Element Method for Hypervelocity Impact Simulation," *International Journal of Impact Engineering*, Vol. 26, 2001, pp. 169–178.

[15] Johnson, G. R., and Stryk, R. A., "Conversion of 3-D Distorted Elements into Meshless Particles During Dynamic Deformation," *International Journal of Impact Engineering*, Vol. 28, 2003, pp. 947–966.

[16] Park, Y.-K., and Fahrenthold, E. F., "A Kernel Free Particle-Finite Element Method for Hypervelocity Impact Simulation," *International Journal for Numerical Methods in Engineering*, Vol. 63, 2005, pp. 737–759.

[17] Johnson, G. R., and Cook H. W., "Fracture Characteristics of Three Metals Subjected to Various Strains, Strain Rates, Temperature and Pressures," *Engineering Fracture Mechanics*, Vol. 21, No. 1, 1985, pp. 31–48.

[18] Curran, D. R., Seaman, L., and Shockey, D. A., "Dynamic Failure of Solids," *Physics Reports*, Vol. 147, 1987, pp. 253–388.

[19] Steinberg, D. J., and Lund, C. M., "A Constitutive Model for Strain Rates from 10^{-4} to 10^{6}/s," *Journal of Applied Physics*, Vol. 65, No. 4, 1989, pp. 1528–1533.

[20] Zerilli, F. J., and Armstrong, R. W., "Dislocation-Mechanics-Based Constitutive Relations for Material Dynamics Calculations," *Journal of Applied Physics*, Vol. 61, No. 5, 1987, pp. 445–459.

[21] Bammann, D. J., Chiesa, M. L., McDonald, A., Kawahara, W. A., Dike, J. J., and Revelli, V. D. "Prediction of Ductile Failure in Metal Structures," *AMD*, Vol. 107, 1990, pp. 7–12.

[22] Camacho, G. T., and Ortiz, M., "Adaptive Lagrangian Modeling of Ballistic Penetration of Metallic Targets," *Computer Methods in Applied Mechanics and Engineering*, Vol. 142, 1997, pp. 269–301.

[23] Borvik, T., Langseth, M., Hopperstad, O. S., and Malo, K. A., "Perforation of 12 mm Thick Steel Plates by 20 mm Diameter Projectiles with Flat, Hemispherical and Conical Noses, Part 1: Experimental Study," *International Journal of Impact Engineering*, Vol. 27, No. 1, 2002, pp. 19–35.

[24] Borvik, T., Clausen, A. H., Hopperstad, O. S., and Langseth, M., "Perforation of AA5083-H116 Aluminum Plates with Conical-Nose Steel Projectiles-Experimental," *International Journal of Impact Engineering*, Vol. 30, 2004, pp. 367–384.

[25] Eftis, J., Carrasco, C., and Osegueda, R. A., "A Constitutive-Microdamage Model to Simulate Hypervelocity Projectile-Target Impact, Material Damage and Fracture," *International Journal of Plasticity*, Vol. 19, 2003, pp. 1321–1354.

[26] Voyiadjis, G. Z., and Abed, F. H., "Microstructural Based Models for BCC and FCC Metals with Temperature and Strain Rate Dependency," *Mechanics of Materials*, Vol. 37, 2005, pp. 355–378.

[27] Voyiadjis, G. Z., Abu Al-Rub, R. K., and Palazotto, A. N., "Non-Local Coupling of Viscoplasticity and Anisotropic Viscodamage for Impact Problems Using the Gradient Theory," *Archives of Mechanics*, Vol. 55, No. 1, 2003, pp. 39–89.

[28] Voyiadjis, G. Z., Abu Al-Rub, R. K., and Palazotto, A. N., "Thermodynamic Formulations for Non-Local Coupling of Viscoplasticity and Anisotropic Viscodamage for Dynamic Localization Problems Using Gradient Theory," *International Journal of Plasticity*, Vol. 20, 2004, pp. 981–1038.

[29] Abu Al-Rub, R. K., Voyiadjis, G. Z., and Palazotto, A. N., "A Micro-Damage Model for High Velocity Impact Using Combined Viscosity and Gradient Localization Limiters," *Proceedings of the ASME Applied Mechanics Division—2005*, Vol. 256, American Society of Mechanical Engineers, New York, 2005, pp. 123–130.

[30] Abu Al-Rub, R. K., and Voyiadjis, G. Z., "A Finite Strain Plastic-Damage Model for High Velocity Impacts Using Combined Viscosity and Gradient Localization Limiters, Part 1: Theoretical Formulation," *International Journal of Damage Mechanics*, Vol. 15, No. 4, 2006, pp. 293–334.

[31] Needleman, A., "Material Rate Dependent and Mesh Sensitivity in Localization Problems," *Computer Methods in Applied Mechanics and Engineering*, Vol. 67, No. 1, 1988, pp. 69–85.

[32] Loret, B., and Prevost, H., "Dynamics Strain Localization in Elasto-(Visco-)Plastic Solids, Part 1: General Formulation and One-Dimensional Examples," *Computer Methods in Applied Mechanics and Engineering*, Vol. 83, No. 3, 1990, pp. 247–273.

[33] Sluys, L. J., "Wave Propagation, Localization and Dispersion in Softening Solids," Ph.D. Thesis, Delft Univ. of Technology, Delft, The Netherlands, 1992.

[34] Wang, W. M., Sluys, L. J., and de Borst, R., "Interaction Between Material Length Scale and Imperfection Size for Localization Phenomena in Viscoplastic Media," *European Journal of Mechanics, A/Solids*, Vol. 15, No. 3, 1996, pp. 447–464.

[35] Molinari, A., "Collective Behavior and Spacing of Adiabatic Shear Bands," *Journal of the Mechanics and Physics of Solids*, Vol. 45, 1997, pp. 1551–1575.

[36] Batra, R. C., and Kim, C. H., "Adiabatic Shear Banding in Elastic-Viscoplastic Nonpolar and Dipolar Materials," *International Journal of Plasticity*, Vol. 6, 1990, pp. 127–141.

[37] Batra, R. C., and Chen, L., "Shear Band Spacing in Gradient-Dependent Thermoviscoplastic Materials," *Computational Mechanics*, Vol. 23, 1999, pp. 8–19.

[38] Batra, R. C., and Wei, Z. G., "Shear Bands Due to Heat Flux Prescribed at Boundaries," *International Journal of Plasticity*, Vol. 22, 2006, pp. 1–15.
[39] ABAQUS, Software Package, Ver. 6.3, Habbitt, Karlsson and Sorensen, Inc., Providence, RI, 2003.
[40] Abu Al-Rub, R. K., and Voyiadjis, G. Z., "Determination of the Material Intrinsic Length Scale of Gradient Plasticity Theory," *International Journal of Multiscale Computational Engineering*, Vol. 2, No. 3, 2004, pp. 377–400.
[41] Abu Al-Rub, R. K., and Voyiadjis, G. Z., "Analytical and Experimental Determination of the Material Intrinsic Length Scale of Strain Gradient Plasticity Theory from Micro- and Nano-Indentation Experiments," *International Journal of Plasticity*, Vol. 20, No. 6, 2004, pp. 1139–1182.
[42] Voyiadjis, G. Z., and Abu Al-Rub, R. K., "Gradient Plasticity Theory with a Variable Length Scale Parameter," *International Journal of Solids and Structures*, Vol. 42, No. 14, 2005, pp. 3998–4029.
[43] Voyiadjis, G. Z., Abu Al-Rub, R. K., and Palazotto, A. N., "On the Small and Finite Deformation Thermo-Elastoviscoplasticity Theory: Algorithmic and Computational Aspects," *European Journal of Computational Mechanics* (to be published).
[44] Zhu, Y. Y., and Cescetto, S., "Fully Coupled Elasto-Visco Plastic Damage Theory for Anisotropic Materials," *International Journal of Solids and Structures*, Vol. 32, 1995, pp. 1607–1641.
[45] Abu Al-Rub, R. K., and Voyiadjis, G. Z., "A Direct Finite Element Implementation of the Gradient Plasticity Theory," *International Journal for Numerical Methods in Engineering*, Vol. 63, No. 4, 2005, pp. 603–629.
[46] Voyiadjis, G. Z., and Abu Al-Rub, R. K. "A Finite Strain Plastic-Damage Model for High Velocity Impacts Using Combined Viscosity and Gradient Localization Limiters, Part 2: Numerical Aspects and Simulations," *International Journal of Damage Mechanics*, Vol. 15, No. 4, 2006, pp. 335–373.
[47] De Borst, R., and Mühlhaus, H.-B., "Gradient-Dependent Plasticity Formulation and Algorithmic Aspects," *International Journal for Numerical Methods in Engineering*, Vol. 35, 1992, pp. 521–539.
[48] De Borst, R., and Pamin, J., "Some Novel Developments in Finite Element Procedures for Gradient Dependent Plasticity," *International Journal for Numerical Methods in Engineering*, Vol. 39, 1996, pp. 2477–2505.
[49] Borvik, T., Hopperstad, O. S., Berstad, T., and Langseth, M. "Numerical Simulation of Plugging Failure in Ballistic Penetration," *International Journal of Solids and Structures*, Vol. 38, 2001, pp. 6241–6264.
[50] Voyiadjis, G. Z., and Abu Al-Rub, R. K., "Thermodynamic Based Model for the Evolution Equation of the Backstress in Cyclic Plasticity," *International Journal of Plasticity*, Vol. 19, 2003, pp. 2121–2147.
[51] Bai, Y., and Dodd, B., *Adiabatic Shear Localization: Occurrence, Theories and Applications*, Pergamon, Oxford, 1992.

T. Nicholas
Associate Editor